

Impedance characteristics of hybrid organometal halide perovskite solar cells

Juan Bisquert, Germà Garcia-Belmonte, Antonio Guerrero

Institute of Advanced Materials (INAM), Universitat Jaume I, 12006 Castelló, Spain

Juan Bisquert, phone 34964727541, email bisquert@uji.es

Germà Garcia-Belmonte, phone 34964727548, email garciag@uji.es

Antonio Guerrero, phone 34964727555, email aguerrer@uji.es

9 February 2016

Contents

Abstract	2
1. Introduction.....	2
2. Capacitive charging and hysteresis	4
3. Ferroelectric properties	12
4. Nature of capacitances in perovskite solar cells: the dark capacitances	13
5. Capacitance-voltage and energy level diagram	17
6. Transient photovoltage and photocurrent	22
6.1. Open-circuit voltage decay	23
6.2. Transient current and charging	25
6.3. Small perturbation illumination methods: Transient photovoltage and charge extraction.	27
7. Reactivity and degradation at electrodes	29
8. The light capacitances	33
Conclusion	35
References.....	37

Abstract

This chapter describes the application of impedance spectroscopy and an array of related experimental techniques used to understand the operation principles of lead halide perovskite solar cells and their related materials. The main topic of the chapter is the identification of capacitances and their origin, which is related to ion accumulation, electron accumulation, or a combination of both. In addition to impedance spectroscopy we examine a number of charging or time transient techniques that are performed by a voltage step or continuous cycling, including capacitance-voltage characterization and Kelvin probe force microscopy. The interpretation is carried out by using several experimental modifications such as use of different contacts, sample thickness, and temperature. The relationship of hysteresis to capacitance is also addressed, as well as the degradation at contacts by ionic accumulation and reaction.

1. Introduction

The research on hybrid organic-inorganic perovskite solar cells is growing rapidly with multiple facets nowadays. Efficiencies for these cells have been rising at a phenomenal speed with a certified value over 21%. A rich variety of fabrication methods have been reported with the aim towards production of low-cost large-scale devices, especially focusing on robust deposition methods and stability of the solar cell. Indeed, an increasing number of composition/configuration types are being investigated and there is a need to clarify optimal preparation methods, i.e. precursors used and preparation routes. These objectives require sound characterization methods that relate the structure of the device to its functioning. At present, it is clear that the hybrid organic-inorganic perovskite materials display a range of fascinating properties that support the extraordinary photovoltaic performance. However, the principles of photovoltaic and photophysical operation are not clear yet in the perovskite photovoltaic devices. A number of key issues hindering further developments need be investigated thoroughly and solved. For a sound understanding of the solar cell device it is necessary to clarify the dynamic processes that occur in the low frequency to intermediate frequency domain and their relationship to materials and structure combinations in the device. This chapter will address the challenging characterization of perovskite solar cell devices using impedance spectroscopy and a variety of related techniques that we describe in the following.

The presence of significant time transient behaviour has been recognized early on in perovskite solar cells and there are varied and complex phenomena that need a suitable classification (Sanchez et al., 2014). There exists a fundamental correspondence between small perturbation decay in time transient techniques and small perturbation ac methods as impedance spectroscopy, therefore in order to establish a coherent picture of perovskite solar cell internal dynamics it is important to combine an array of experimental methods as indicated in Fig. 1.

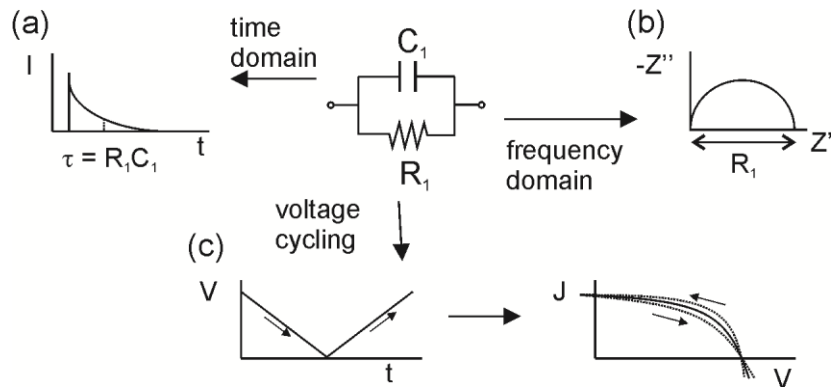


Fig. 1. Parallel RC equivalent circuit, and the experimental signatures in time and frequency domain. (a) Current density decay after a step voltage. (b) Impedance spectroscopy. (c) Voltage cycling leading to current density-voltage curve.

When a physical element $R_1 C_1$ as shown in Fig. 1 is perturbed with a step voltage, the electric current decays with exponential shape defined by the characteristic time

$$\tau = R_1 C_1 \quad (1)$$

as indicated in (a). If the perturbation is ac voltage, the relation ac voltage to current is a complex impedance, Z . For the parallel circuit in Fig. 1, the impedance spectrum traces a semicircle in the complex plane as shown in Fig. 1b. In addition a continuous change of voltage outlined in c, shows important information as capacitive components and the steady state current density-voltage ($J - V$) curve.

In this chapter we describe the application of these techniques in order to obtain a detailed picture of the operation of perovskite solar cells, based on $\text{CH}_3\text{NH}_3\text{PbI}_3$ (or MAPI_3) and their multiple compositional variants. The structure of the cell is formed by perovskite absorber and selective contacts for extraction of electrons and holes as shown in Fig 2a. Additional energetic features as band bending will be discussed later on. Particularly important in the study of perovskite solar cells has been the ability to use a variety of contact types, which often modify drastically the performance and properties of perovskite solar cells. As shown in Fig. 2 one may distinguish several typical configurations depending on the contacts: (a) planar or (b) mesoporous metal oxide layer at the transparent side, or use a hole conductor at the transparent side, (c) (“inverted” structure). The use of symmetric devices (d, e) has produced very large rewards in terms of understanding as discussed in section 7.

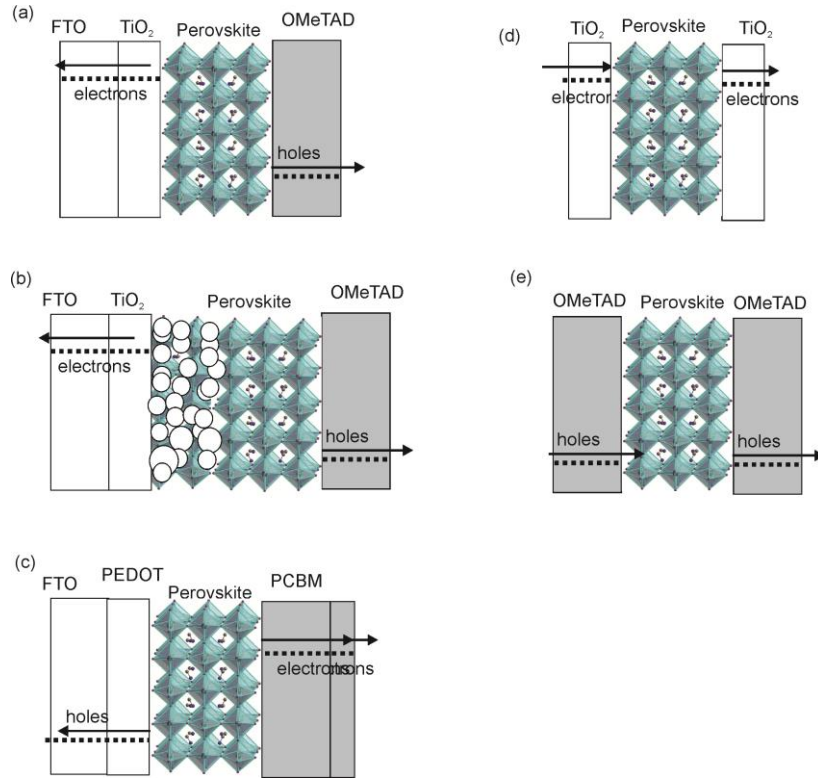


Fig. 2. Different types of samples configurations. (a-c) diode configuration (solar cell) with (a) mesoporous and (b) planar metal oxide layer at the transparent side. (c) “inverted” structure with a hole conductor at the transparent side. (d, e) Symmetric devices with electron selective contacts (d) and hole selective contacts (e).

2. Capacitive charging and hysteresis

In the analysis of solar cells, impedance and time transient small perturbation measurement have been widely used for the determination of devices characteristics and lifetimes (Bisquert and Fabregat-Santiago, 2010, Fabregat-Santiago et al., 2011). However, the central type of measurement in solar cells is the $J-V$ curve at steady state. From this curve the main parameters that characterize solar to electricity conversion characteristics at steady state operation are extracted: photocurrent, photovoltage, fill factor, and power conversion efficiency. This measurement requires a nearly continuous voltage scan, which is carried out at certain voltage steps, with simultaneous measurement of current, as indicated in Fig. 2c. The scan can begin at the value of open circuit voltage, V_{oc} , towards the point of $V = 0$, that is from forward to reverse bias, or the other way around. If the step size ΔV take a time interval Δt , then the scan rate is

$$s = \frac{\Delta V}{\Delta t} \quad (2)$$

This procedure is the same as in the standard technique of cyclic voltammetry in electrochemistry. It is important to recall the behaviour of a capacitor in this type of

measurement (Fabregat-Santiago et al., 2003). For a single constant capacitor C the charging current is obtained by time derivative of the charge in the capacitor,

$$J_C = \frac{dQ}{dt} = C \frac{dV}{dt} \quad (3)$$

and the result is

$$J_C = C s \quad (4)$$

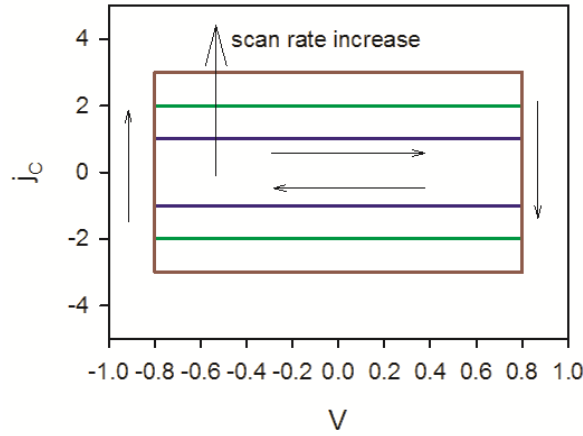


Fig. 3. Capacitive current resulting from cycling the voltage applied to the capacitor at increasing scan rates.

As observed in Fig. 3, by cycling the voltage between two points, capacitive charging produces a current that is proportional to scan rate s , and furthermore the current is inverted when the scan direction changes sign. Therefore the signature of capacitive current is a symmetric current with respect to the average value. For a single capacitor the average value is 0 as indicated in Fig. 3. But in general the capacitive current is added to other dc currents existing in the system. For a solar cell, the steady state dc current is well characterized (neglecting internal resistances) by a photocurrent and diode curve of the form

$$J = J_{ph} - J_0 \left(e^{qV/mk_B T} - 1 \right) \quad (5)$$

Here j_{ph} is the photocurrent density, j_0 is the dark current density, q is elementary charge, $k_B T$ is the thermal energy, and m is the diode quality factor. In consequence, the total current under voltage scan in a solar cell will be given by the addition of the characteristic (5), with capacitive current added or subtracted according to forward or reverse scan, respectively, as suggested by (Sanchez et al., 2014). The result is shown in Fig. 4d, where it is observed that the separation from steady state curve (the central curve, made at very slow scan rate) increases with voltage speed, as indicated in Fig. 3. This is the mark of capacitive hysteresis (Chen et al., 2015).

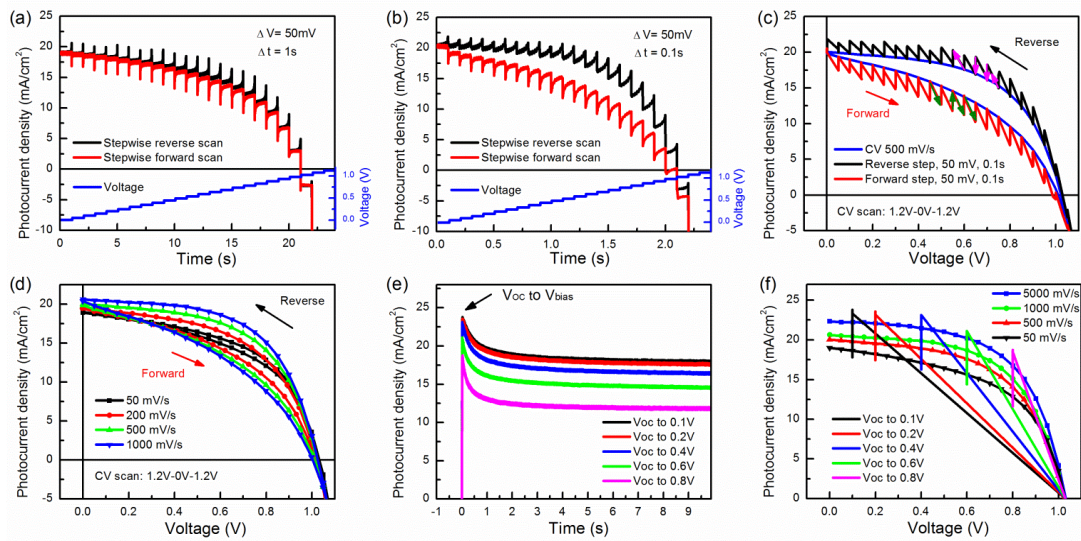


Figure 4. Time transients of a perovskite solar cell formed by mesoporous (mp) TiO_2 electron contact, with 500 nm $\text{CH}_3\text{NH}_3\text{PbI}_3$ film as the light absorber layer and 150 nm Spiro-OMeTAD as the hole selective layer. Time-dependent photocurrent response under reverse and forward stepwise scans with (a) 1 s step time and (b) 0.1 s step time. (c) J - V response for the CV scan with 500 mV/s and corresponding stepwise scan. (d) J - V response for PSCs with different CV scan rates. (e) Dynamic photocurrent transient when switching the applied voltage from V_{oc} to different bias. (f) J - V response for the different reverse scans and dynamic photocurrent transient in (e). Reprinted from (Chen et al., 2015).

In order to describe in more detail the capacitive charging of the solar cell one needs to observe the transient current for each voltage step as in Fig. 5. In this figure the response of devices with two different hole selective contacts, spiro-OMeTAD and CuI, are compared (Sepalage et al., 2015). Obviously for the second case the transients are much shorter than for spiro-OMeTAD, which is related to a smaller capacitance influencing the decay time as indicated in Fig. 1a. The low frequency capacitance measured in these cells is shown in Fig. 6b. Similarly, the measurements in Fig. 4a and b illustrate the effect of capacitive current upon J - V curve. When the scan rate is slow (large Δt) as in Fig. 4a, the current has sufficient time to reach steady state value corresponding to Eq. (5) (Kim and Park, 2014, Unger et al., 2014). However, under fast scan rates Δt leaves the current on a transient value before the next voltage step comes in, so that the overall current stays above the stationary value, as shown in Fig. 4b. As expected the opposite sign of capacitive current occurs in the reverse scan, causing the opening of current with respect to steady state value. This behaviour depends on the scan rate indicated in Eq. (2) and not on separate values of Δt and ΔV , provided both are relatively small. Thus two different procedures are applied in Fig. 4c and they provide the same amount of capacitive hysteresis.

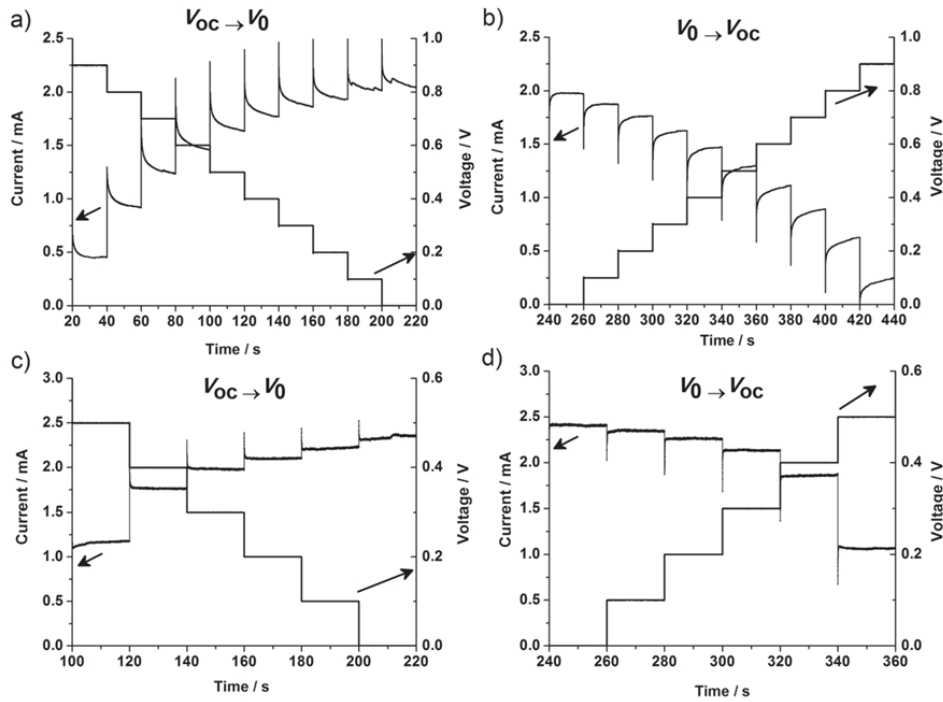


Fig. 5. Time transients using forward and reverse stepwise voltage sweeps for a perovskite solar cell formed by 50 nm planar TiO_2 electron contact, with 300-400 nm $CH_3NH_3PbI_3$ film as the light absorber layer, and two different hole selective contacts, (a, b) spiro-OMeTAD and (c, d) CuI. Reprinted from (Sepalage et al., 2015).

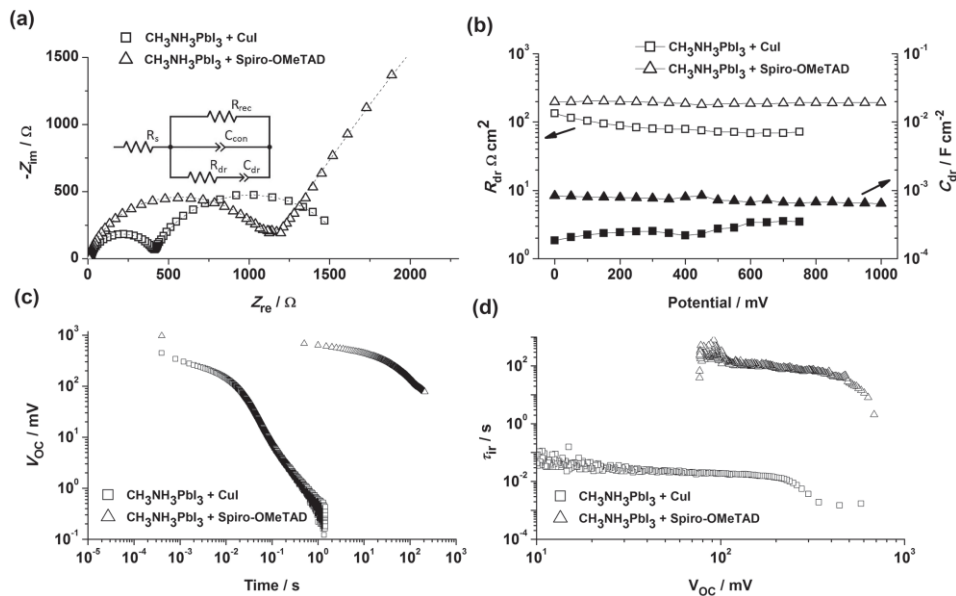


Fig. 6. (a) Complex plane impedance plots obtained for a CuI-based solar cell device (circles) and a Spiro-OMeTAD-based device (squares). Fits are shown in the dashed lines and the equivalence circuit used for fitting the impedance response is provided in

the inset. (b) Variation in resistance and capacitance as a function of potential for both devices. Impedance measurements were performed under constant illumination. (c) OCVD measurements for CuI-based and spiro-OMeTAD-based devices; and (d) their corresponding instantaneous relaxation time constants, τ_{ir} , as a function of the V_{oc} . Reprinted from (Sepalage et al., 2015).

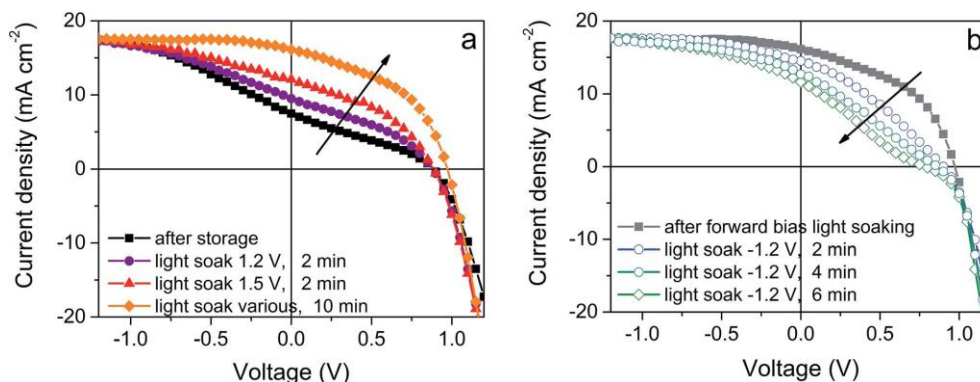


Fig. 7. (a) Light-soaking at forward bias positively affects the current–voltage and hence the performance of thin film perovskite-absorber solar cells. The solar cells are formed by mesoporous (mp) TiO₂ electron contact, with 350 nm CH₃NH₃PbI₃ film as the light absorber layer and 150 nm Spiro-OMeTAD as the hole selective layer. (b) The reverse effect is observed after light soaking under reverse bias conditions with the IV-curves developing an S-shape. Reprinted from (Unger et al., 2014).

In addition to the capacitive hysteresis, another type of hysteresis has been widely reported, that depends not only on scan rate, but on previous pretreatments. Examples are shown in Fig. 7, that reveal that light soaking at forward bias improves the $J - V$ characteristic, while light soaking at reverse bias has the opposite effect (Unger et al., 2014). These results indicate the dramatic changes that occur in the perovskite solar cell devices when light and voltage have been applied (Sanchez et al., 2014, Chen et al., 2015, Gottesman and Zaban, 2016).

Importantly, it has been widely reported that the lead halide perovskite is a good ionic conductor, in which interstitials and vacants can move under internal forces (Azpiroz et al., 2015). Ionic movement of I⁻ and MA⁺ have been reported to take place under applied bias and/or illumination conditions (Eames et al., 2015, Yang et al., 2015). The drift of ions and/or vacancy turns the lead halide perovskite into a mixed ionic-electronic conductor which creates a number of complexities of interpretation of electrical measurements as outlined in Fig. 8. When a bias voltage is applied to the asymmetric device, it is induced the displacement of different carriers, ionic and electronic. However, whilst either type of electronic carrier can be transported through the solar cells contacts ionic carriers are blocked, so that in dc regime the ionic current is suppressed. This means that the electrochemical potential of ions must be constant, which implies a concentration gradient in opposite sense to the electrical field drift as

explained by (Hebb, 1952). Fig. 9 shows the study of galvanostatic charging of a thick symmetric sample at a constant current of 2 nA. Initially the current is maintained by both electronic and ionic current, but as an ionic gradient is established the ionic current is suppressed and more voltage is necessary to maintain the value of the current, that is purely electronic (Yang et al., 2015). Strong evidence for the effects of ionic migration over contact barriers has been provided by (Xiao et al., 2015), see Fig. 10, who showed that short time polarization of the perovskite layer can determine the contact type as hole or electron selective layer, independently of the type of metal contact. This type of inversion of $J - V$ characteristics with respect to the type of contacts is widely reported in ferroelectric materials, and it is usually associated to the migration of defects or polarization changes that modify the injection barriers at contacts (Lee et al., 2011). Reactivity between these moving ions and external contacts can dramatically impact the solar cell operation and stability as further discussed in section 7.

Another widely reported observation is the large dependence of hysteresis on the type of contacts has been observed as shown in examples in Fig. 11. Such changes are strongly correlated with the low frequency capacitance as indicated in Fig. 12 (Kim et al., 2015).

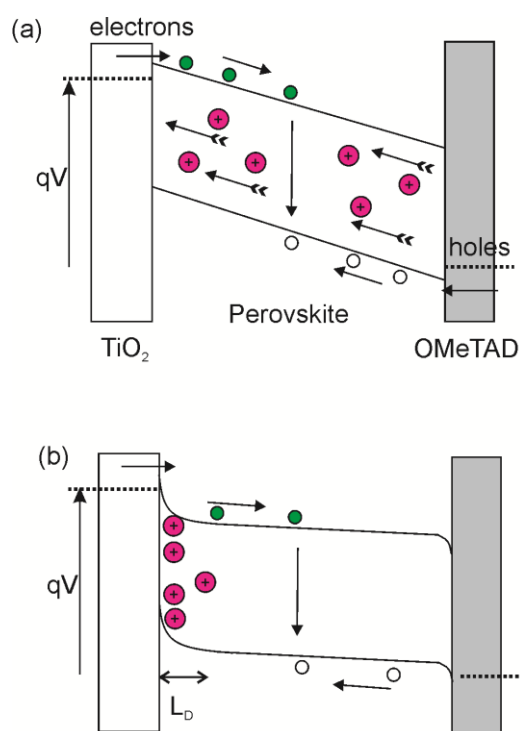


Fig. 8. Schematic diagrams indicating the different components of electric current in asymmetric perovskite device in the dark. (a) Starting from homogenous situation, forward applied bias voltage V a drift field that causes the displacement of positively charged I^+ vacants. The electronic current is produced by injection of electrons and holes at the respective contacts and recombination inside the perovskite layer. Note that ionic

and electronic currents are marked by different types of arrows. (b) After a certain time the ionic drift causes accumulation of ions at the cathode that produces space charge and a diffusion current against the drift field. Eventually an equilibrium distribution of ions mainly at the cathode surface is obtained that will be controlled by the ionic Debye length L_D as indicated. Meanwhile the electronic recombination current persists as long as the voltage is applied.

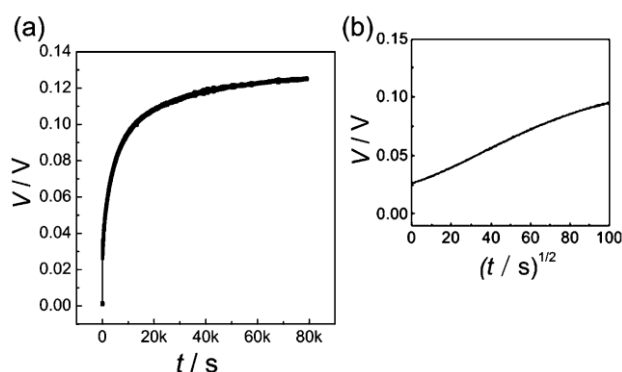


Fig. 9. (a) DC polarization curve for a symmetric graphite/MAPbI₃/Graphite cell (thickness 0.6 mm) measured at 308 C in Ar flow by applying a current of 2 nA. (b) Voltage versus square root of time up to 104 seconds. Reprinted from (Yang et al., 2015).

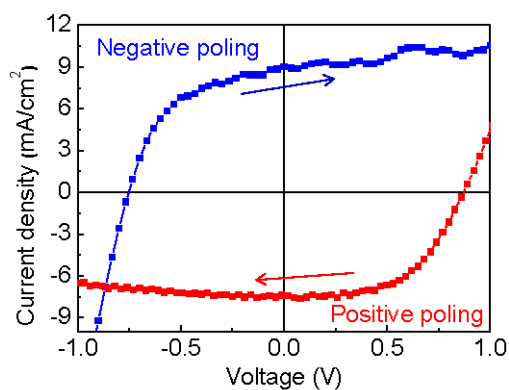


Fig. 10. Performance variation of ITO/PEDOT:PSS/Perovskite (300 nm)/Au vertical structure devices. The devices were poled at 6 V/ μ m for 20 s. The photocurrents were measured under 1 sun illumination at a sweep rate of 0.14 V/s. Reprinted from (Xiao et al., 2015)

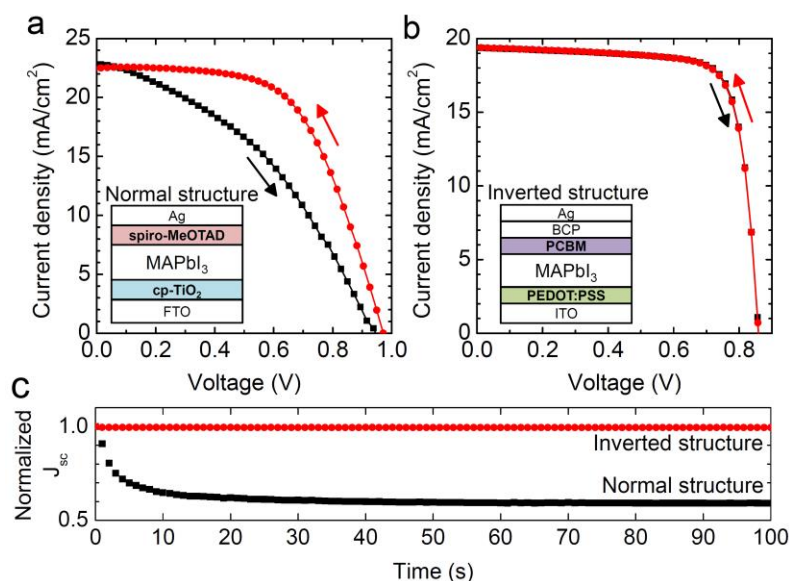


Fig. 11. J-V hysteresis and time-dependent photocurrent. (a) scan direction-dependent J-V curves of the planar-TiO₂/MAPbI₃/spiro-MeOTAD (normal) structure and (b), the PEDOT:PSS/ MAPbI₃/PCBM (inverted) structure. During J-V scan the current was acquired for 100 ms after applying a given voltage. (c) Normalized time-dependent J_{sc} of the normal and the inverted structures. Open-circuit condition under one sun illumination was maintained before measuring J_{sc}. Reprinted from (Kim et al., 2015).

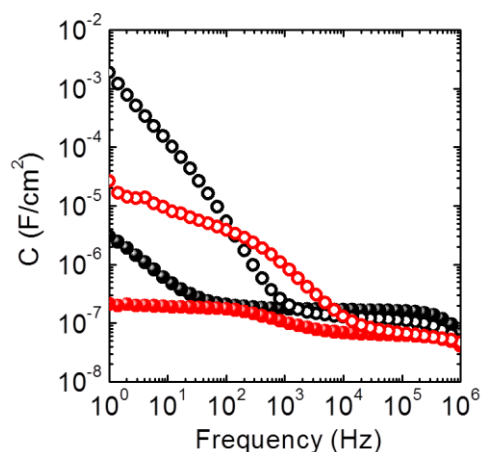


Fig. 12. Frequency dependent capacitance C - f curves of the planar-TiO₂/MAPbI₃/spiro-MeOTAD (normal, black) structure, thickness 440 nm and the PEDOT:PSS/ MAPbI₃/PCBM (inverted, red) structure, thickness 380 nm, in dark (filled symbols) and under one sun illumination at short-circuit condition (bias voltage = 0 V, empty symbols). Reprinted from (Kim et al., 2015).

3. Ferroelectric properties

Ferroelectric materials are characterized by a permanent electrical polarization. A typical phase transition to a nonferroelectric symmetric crystal phase occurs at the Curie temperature, where the macroscopic polarization ordering cannot be maintained. The transition is accompanied by a large variation the dielectric constant. The polarization field can switch direction by an applied external field. In ferroelectric layers with metallic contacts the charges in the electrode compensate the bound polarization charge, which removes the internal polarization field. In practice ferroelectric materials can maintain internal electrical fields due to imperfect screening of polarization charge which creates an internal depolarization field.

As many perovskites are ferroelectric, in early studies of organic-inorganic photovoltaic perovskites the ferroelectric property was an appealing explanation of some exotic observations, for example very large dielectric constant, which are typical of oxide perovskites. In lead halide perovskite, three main mechanisms of polarization are expected: the orientational polarization of MA^+ cation (which has significant dipole moment), the ionic polarization induced by the shift of the positive charge center of MA^+ relative to the negative charge center of the PbI_3^- cage, and the ionic polarization induced by the off-center displacement of Pb within the PbI_6 octahedra. In order to determine the interest of such important property for the photovoltaic function, (Coll et al., 2015) utilized piezoelectric force microscopy (PFM), which is a variant of AFM that is widely used to image polarization structure and local switching in ferroelectric materials. The study of MAPbI_3 perovskite films showed piezo-phase hysteresis loops as seen in Fig. 13a. In principle this observation is evidence for ferroelectric polarization, but in contrast to a standard material as BiFeO_3 , the polarization in the lead halide perovskite thin film vanishes in a matter of seconds. It is also observed that the coercivity is greatly enhanced under illumination, which would indicate the presence of a light enhanced dipole (Wu et al., 2014).

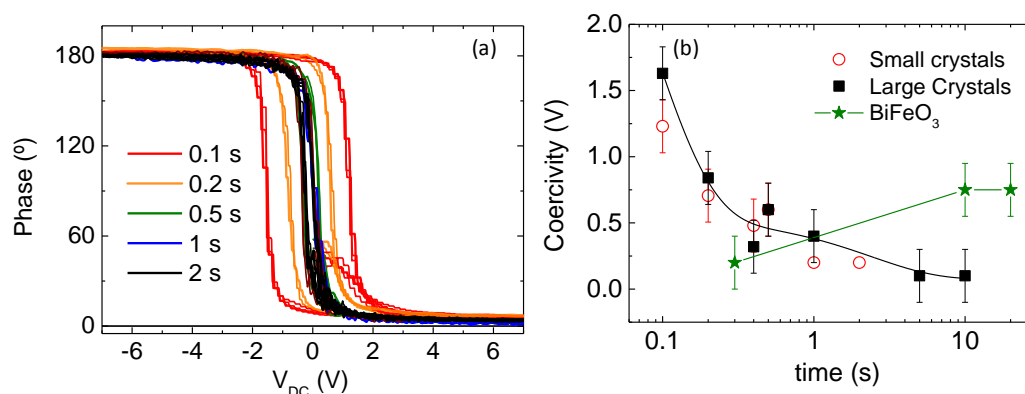


Fig. 13. (a) Piezo-phase hysteresis loops of MAPbI_3 thin films with small crystals performed at different acquisition times. (b) Coercivity dependence with time of MAPbI_3 films with small (red open circles) and large crystals (black squares) and 25 nm

BiFeO_3 thin films (green stars). Reproduced from (Coll et al., 2015).

Another important effect that produces evidence for ferroelectric property is the observation of hysteresis in the cycling of polarization P with respect to voltage (or field). Since measurement of polarization is based on the integrated charge from the current, an internal leakage current completely masks the displacement current due to reordering of ferroelectric domain. This effect plagues the observation of ferroelectric hysteresis and is expected to be large for a large conductivity sample. Indeed (Fan et al., 2015) measured polarization dependence on applied field and failed to find ferroelectric loops but instead attributed the results to leakage currents. In the samples of (Coll et al., 2015) only capacitive response was observed, but not hysteresis in the $P-V$ plot.

Being MA^+ the main polarization mechanism, the permanent polarization of MAPI_3 is due to alignment of MA cation molecules. The weak ferroelectricity of MAPbI_3 described above is in agreement with several theoretical and experimental works which indicate that the molecule is fully activated and free to rotate at room temperature (Poglitsch and Weber, 1987, Onoda-Yamamuro et al., 1990, Mosconi et al., 2014, Fan et al., 2015, Leguy et al., 2015, Mattoni et al., 2015). The observed trends of polarization have been explained by computations of polarization ordering in tetragonal and orthorhombic phases (Fan et al., 2015, Filippetti et al., 2015). The ferroelectric ordering is effective only when the barrier for rotation of MA becomes significant, below 160 K, when the transition from tetragonal to orthorhombic occurs. This is why at room temperature the poling provides no significant image inversion (Kutes et al., 2014, Kim et al., 2015). Therefore ferroelectric property does not seem to play a central role in electric and photoelectric behavior of the most widely used organic-inorganic perovskites. However, it is not yet known if the strong polar character of the perovskites is a central attribute to the excellent photovoltaic performance of these materials, e.g. via formation of polarons (Zhu and Podzorov, 2015).

4. Nature of capacitances in perovskite solar cells: the dark capacitances

Interpretation of capacitance in perovskite solar cells is complicated by the wide variety of possible phenomena that can potentially cause capacitance response. The classification of these effects has been summarized in (Bisquert et al., 2016). In brief, main aspects of the capacitance include: Dielectric capacitance, chemical capacitance, depletion layer at contact barrier (or possibly accumulation or inversion capacitances), and electrode polarization, consisting on ionic accumulation at the interface.

The main characteristics of measured capacitance in perovskite solar cells, have been described previously (Juarez-Perez et al., 2014, Almora et al., 2015) and are shown in Fig. 12 and 14. The capacitance in dark at room temperature is characterized by a high frequency plateau that rises towards very large values as the frequency is reduced. The plateau is more or less visible depending on the onset of the low frequency capacitance,

see Fig. 11. Under illumination there is a very large increase of the low frequency capacitance as indicated in Fig. 12 and 14, and these effects will be discussed in a separate section of this chapter.

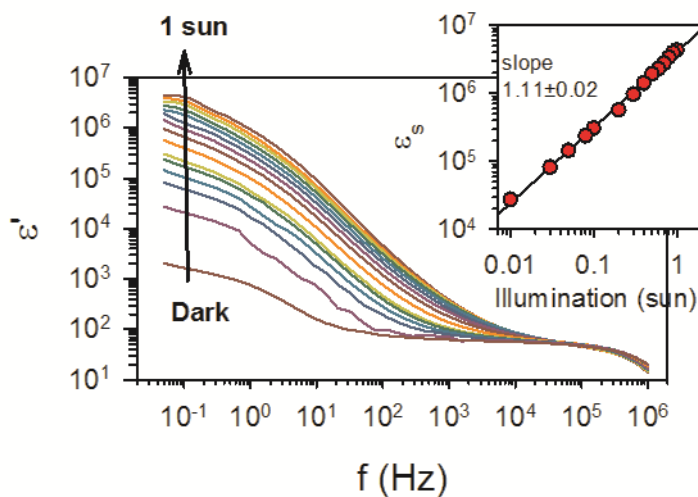


Fig. 14. Plot of the real permittivity as a function of frequency for different incident light intensity (Φ_0) from dark to 1 sun, for $\text{TiO}_2/\text{meso-Al}_2\text{O}_3/\text{CH}_3\text{NH}_3\text{PbI}_{3-x}\text{Cl}_x/\text{OMeTAD}/\text{Au}$ perovskite solar cell. Measurements have been carried out at room temperature and 0 V applied bias. Inset, linear regression of the dielectric constant at $f = 50$ mHz vs. illumination intensity, observing a close to linear dependence between ϵ_s and intensity of illumination. Reprinted from (Juarez-Perez et al., 2014).

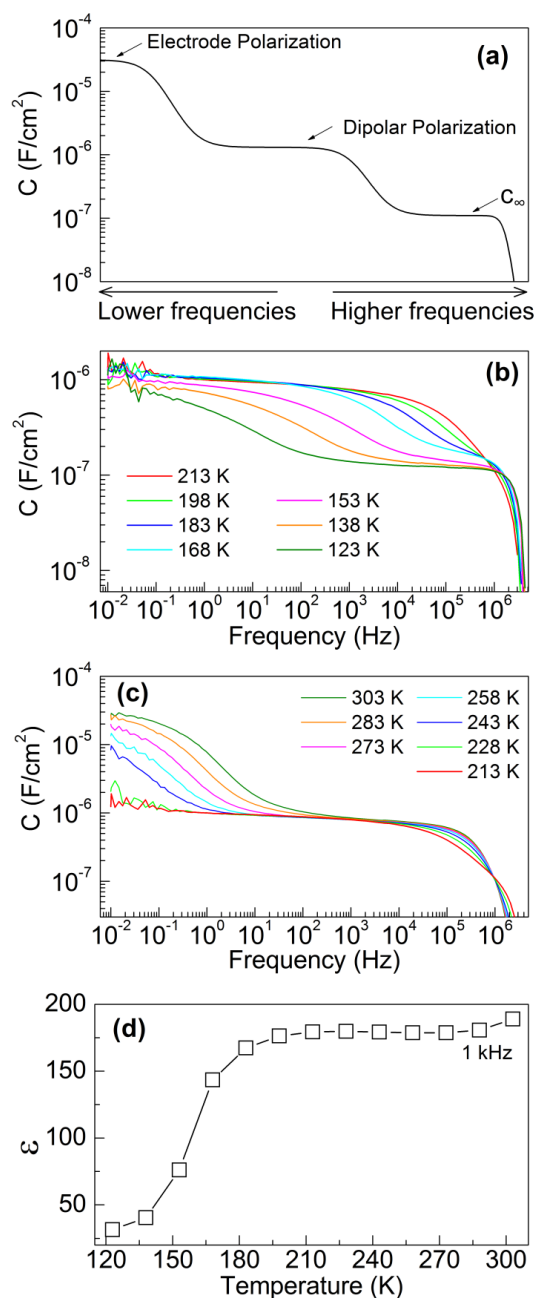


Fig. 15. Capacitance vs. frequency at different temperatures (dark) of a perovskite solar cell formed by planar TiO₂ electron contact, with 400 nm CH₃NH₃PbI₃ film as the light absorber layer and 150 nm Spiro-OMeTAD as the hole selective layer. Reprinted from (Almora et al., 2015).

The universal shape of capacitance dependence on frequency is composed of a series of plateaus. In between the plateau we obtain capacitance increments associated to different relaxation processes that determine the kinetics of each capacitance. At low frequencies all capacitive processes contribute but they are progressively cancelled when moving to high frequencies (Bisquert et al., 2016). Therefore the general shape of capacitance plot has the form of Fig. 15a and the separate steps need to be physically

characterized. However, the presence of frequency dispersion complicates this task. In this case a constant phase element (CPE) $Z = Q(i\omega)^{-n}$, where Q is a prefactor and $0 \leq n < 1$ is a constant exponent, replaces the capacitor. The capacitive impedance of this type provides a steady increment of $C(f)$ that masks the plateaus (Bisquert et al., 2016). Thus the light curves in Fig. 14 have a steady decrease that is held up to very high frequencies, which forms a featureless spectrum that is hard to analyse. Major progress in the understanding the dark capacitance has been obtained by measuring samples with modified thickness and temperature. Cooling the sample has revealed the nature of capacitive steps, as shown in Fig. 15b and c. It has thus been possible to separate: (i) the bulk polarization associated to dielectric relaxation of the sample, from (ii) the low frequency capacitance. This large low frequency capacitance has been largely ascribed to contact phenomena, in congruence with the hysteresis behaviour described in the previous section.

The accumulation of ions at the contact interface produces a capacitance due to surface space charge, that responds in the low frequency range of the measurement in ordinary ionic conductors (Beaumont and Jacobs, 1967, Tomozawa and Shin, 1998, Lunkenheimer et al., 2002). This capacitance occurs in a short distance to the contact and it is independent of the active film thickness d , as indicated in Fig. 8b. Electrode polarization gives rise to capacitances of order $10 \mu\text{F cm}^{-2}$, and can be modeled following the classical Gouy-Chapman double-layer model (Kim and Tomozawa, 1976), (Almora et al., 2016).

$$Q_{\text{diff}} = \frac{2\varepsilon_0 k_B T}{qL_D} \sinh\left(\frac{q\Delta\phi}{2k_B T}\right) \quad (6)$$

Q_{diff} corresponds to the charge per unit area, $\Delta\phi$ is the potential drop between the metallic contact and the absorber bulk, and the ion Debye length is given by

$$L_D = \sqrt{\frac{\varepsilon_0 k_B T}{q^2 N}} \quad (7)$$

Here N accounts for the density of ionic charges. By derivation with respect to the potential, Debye capacitance C_D is obtained at $\Delta\phi = 0$:

$$C_D = \frac{\varepsilon_0}{L_D} \quad (8)$$

In equilibrium (zero bias) and room temperature, excess ion carriers accumulate within an extension (space charge region) equivalent to the Debye length.

In addition to the low frequency features, as observed in Fig. 14 for measurement under dark at zero bias, capacitance spectra of $\text{MAPbI}_{3-x}\text{Cl}_x$ -based planar devices show two steps appearing at low temperatures (120-180 K), and high temperatures (180-320 K), respectively, that are interpreted in terms of bulk perovskite polarization processes. The dielectric polarization has two main origins that compose the true dielectric constant ε of the perovskite material. First we have the dipolar relaxation mechanisms, that have

been already indicated above in terms of ionic process: MA^+ cation rotation, the shift of MA^+ center relative to PbI_3^- cage, and the off-center displacement of Pb. In addition, when all atoms are frozen at higher frequencies ($>1\text{GHz}$), electronic polarization phenomena exist that cause a small fraction of the low frequency dielectric constant.

A number of papers reported previously the dielectric properties of lead halide perovskites. Work by (Poglitsch and Weber, 1987) measured effective dielectric constant for MAPbI_3 at 300 K to be 33 at a frequency of 90 GHz. Other reports (Onoda-Yamamuro et al., 1992) provided a value of ca. 58 at a frequency of 1 kHz. In contrast, the dielectric constant, *in the absence of molecular reorientation*, is predicted to be 24.1 from electronic structure calculations (PBEsol+ QSGW) (Brivio et al., 2014) in good agreement with the value of 23.3 determined from a fit of permittivity measurements over 100–300 K to the Kirkwood-Fröhlich equation.

The *high-frequency plateau* observed in Fig. 15b ($C = 100 \text{ nF cm}^{-2}$) can be related to the perovskite permittivity of the orthorhombic phase dominating at low temperature in combination with the dielectric contribution of contacts layers as *spiro*-OMeTAD and TiO_2 . Fig. 15 also allows us to extract conclusions regarding the temperature variation of dielectric constant. Lead halide perovskite MAPbX_3 ($\text{X}=\text{Cl}$ or Br) crystals undergo a phase transformation at ~ 160 K between orthorhombic (γ -phase with $\varepsilon \approx 24$) and tetragonal (β -phase with $\varepsilon \approx 55$ at 300 K) structures (Masaki et al., 1997). Fig. 15d shows that the phase transformation provokes a large increase of the dielectric constant that is observed when measuring the capacitance spectra of complete perovskite-based solar cells, in agreement with the literature based on symmetric samples. The low-temperature increment in Fig. 15c yields a permittivity value for the β -phase of $\varepsilon = 32.5$ at 300 K, in good agreement with other reports (Brivio et al., 2013, Frost et al., 2014). It should be noted that a considerable extent of disparity is found among reported permittivity values ($\varepsilon \approx 24-55$). Due to the fact that perovskite films are polycrystalline and that TiO_2 layer is in some cases mesoporous, one can expect roughness factors as high as 3-5, as pointed out by (Pockett et al., 2015). Alternatively, when a voltage is applied towards positive bias (forward) the capacitance increases and this increase has been correlated with the modulation of a depletion capacitance as it will be described section 5.

These observations are summarized in Fig. 15a that identifies the general structure of dark capacitance features in lead halide perovskite layers.

5. Capacitance-voltage and energy level diagram

Different mechanisms of collection efficiency in photovoltaic devices are determined by the carrier conductivities, diffusion length, and the electrical field distribution within the semiconductor material that combines diffusion transport with drift transport (Kirchartz et al., 2015). Charge transport of minority carriers throughout quasi-neutral zones occurs by diffusion in the bulk of the semiconductor. On the other hand, drift governs the carrier motion within the band bending regions close to the external

contacts. The energetic offset between work functions of absorber and each contact material generates a built-in voltage V_{bi} in equilibrium conditions (Fig. 16a). Importantly, several profiles may be formed depending on the type of dopant, doping density and applied voltage.

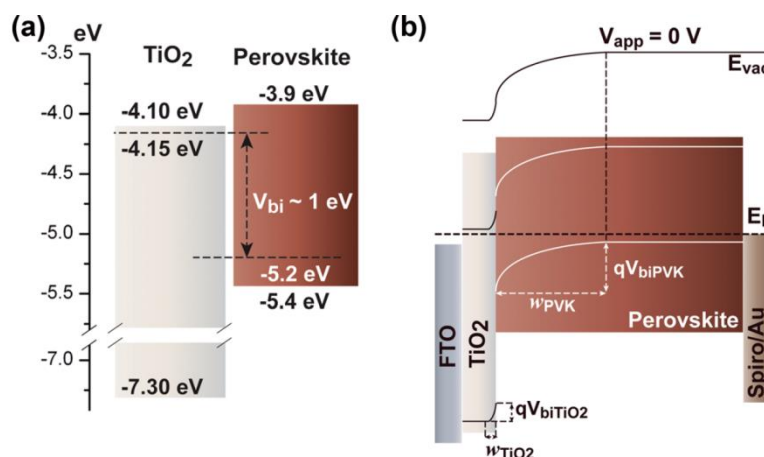


Fig. 16. (a) Illustrative energy diagram of TiO₂ and PVK. A built-in voltage approximately equal to 1 eV is expected. (b) Band diagram in equilibrium showing the formation of a *p-n* (perovskite-TiO₂) type heterojunction. Reproduced with permission from (Guerrero et al., 2014).

Two techniques are especially useful to probe the electrical profile close to the contacts: Kelvin Probe Force Microscopy (KPFM) and Capacitance-Voltage (*C-V*). KPFM allows the direct observation and mapping of the electrical field distribution in a device. Alternatively, *C-V* is an indirect technique where by measuring the capacitance of the semiconductor one can infer the doping density of defects and voltage at which bands are flat (Guerrero et al., 2012). The operation principle of a *C-V* measurement is similar to that of impedance spectroscopy but the analysis is restricted to a single frequency during the ac perturbation. Capacitance-voltage measurement is a useful non-destructive technique to discriminate between effects taking place at the bulk of active layer and those occurring at the interfaces with the external contacts (Guerrero et al., 2013, Guerrero et al., 2014). Fig. 17 shows the *C-V* analysis applied to a degradation experiment of perovskite solar cells.

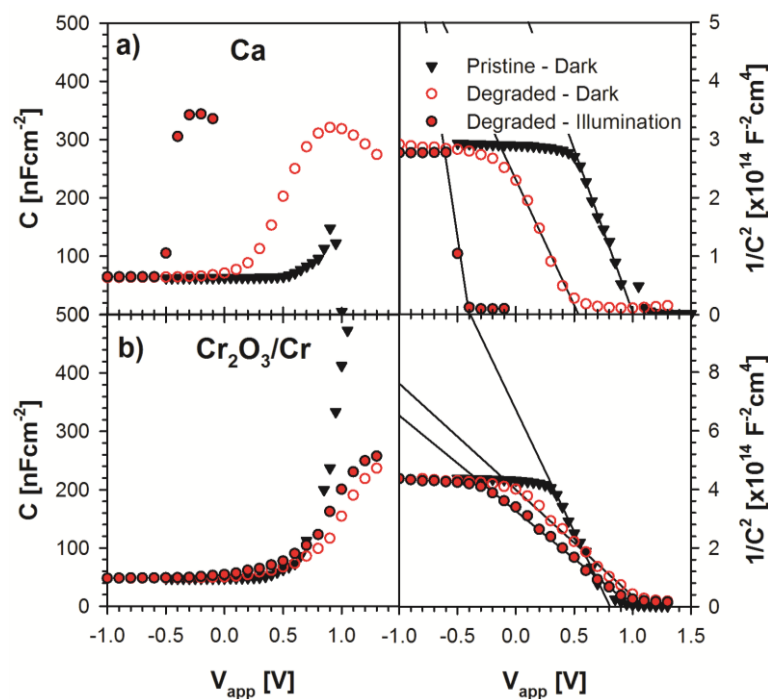


Fig. 17. Capacitance-Voltage and Mott Schottky plots measured during degradation studies for devices in the configuration ITO/PEDOT:PSS/Perovskite/PCBM/Metal, (a) Ca and (b) $\text{Cr}_2\text{O}_3/\text{Cr}$. Reproduced with permission from reference (Guerrero et al., 2015).

By coupling of both techniques, perovskite devices have been shown to contain *p*-type defects and a *p-n* heterojunction is formed with the TiO_2 external contact (Fig. 16) (Guerrero et al., 2014), (Jiang et al., 2015) also observed this type of heterojunction at the electron selective contact and a large depletion layer which indicates that drift of minority carriers is necessary despite the long diffusion length generally reported in perovskite layers.

It has been noted in section 4 that the capacitance in the high frequency region is related to the perovskite permittivity. Indeed, full depletion occurs at negative (reverse) applied voltage and at short circuit conditions for good performing devices ($\sim 16\%$ PCE) as the pristine devices shown by (Guerrero et al., 2015) in Fig. 17. However, as the voltage is applied towards positive bias (forward) an increase in the capacitance is observed. This increase in capacitance is correlated to the width of the depletion zone of a Schottky barrier at the cathode, as supported by Kelvin Probe measurements (Guerrero et al., 2014). The depletion zone decreases at positive bias voltage and as a consequence the capacitance increases, and by plotting $C^{-2}(V)$ a straight line is observed. The density of fully ionized defect states (*p*-doping level) N is derived from the slope by means of the Mott–Schottky relation

$$C^{-2} = \frac{2(V_{fb} - V)}{A^2 q \epsilon \epsilon_0 N} \quad (1)$$

where V_{fb} is the voltage at which bands are flat and A the device active surface.

Doping alters the electrical field distribution by the presence of charged impurities or defects of structural or chemical origin introduced during device processing. In addition, defects may pose a detrimental effect on the solar cell performance as it has been shown by investigating the diode behavior of perovskite solar cells that trap-assisted recombination via electron traps is present as a non-radiative loss mechanism (Wetzelaer et al., 2015). Photovoltaic devices where only direct free-carrier recombination occurs show diode ideality factors close to 1 (Chih-Tang et al., 1957). Alternatively, if trap-assisted recombination is present the diode ideality factor increases to values close to 2 and this has indeed been observed for perovskite solar cells with applied voltages in the range of 0.7-1.0 V (Wetzelaer et al., 2015).

Importantly, it needs to be clarified that neutral vacancy pair defect (Schottky defects), such as PbI_2 and $\text{CH}_3\text{NH}_3\text{I}$ vacancy, do not account for a trap state, which would reduce carrier lifetime (Wang et al., 2014). Alternatively, elemental defects (Frenkel defects) like Pb, I, and CH_3NH_3 vacancies act as dopants, which explains the unintentional doping of methylammonium lead halides (Kim et al., 2014). It has also been proved that the n -/ p -type can be efficiently manipulated by controlling growth processes. For example, (Wang et al., 2014) have reported that an excess of MAI produces p -type character defects by having Pb^{2+} vacancies. Alternatively, an excess of PbI_2 induces generation of n -type defects by having I vacancy. Interestingly, thermal annealing can convert the p -type perovskite to n -type by removing MAI. In addition, the deposition method also influences the amount of defects as this will determine the crystallinity and the defects confined to the grain boundary.

A clear correlation of the charge carrier mobility with perovskite domain size has been observed by using time-resolved microwave conductivity measurements (Fig. 18) (Oga et al., 2014). Defects measured in complete photovoltaic devices represent extremely shallow traps with depth in the order of 10 meV that allow the achievement of extremely high charge carried mobilities with minimum values of up to $20 \text{ cm}^2 \text{ V}^{-1} \text{ s}^{-1}$ attributed to holes for devices prepared using a 2-step process on mesoporous TiO_2 . Under best preparation conditions intrinsic mobilities of each PVK sample of 60–75 $\text{cm}^2 \text{ V}^{-1} \text{ s}^{-1}$ were obtained. Exceptionally low trap-state densities on the order of 10^9 to 10^{10} cm^{-3} are obtained for single crystal materials which show long carrier diffusion lengths exceeding 10 μm and high mobility $115 \text{ cm}^2 \text{ V}^{-1} \text{ s}^{-1}$ (Shi et al., 2015).

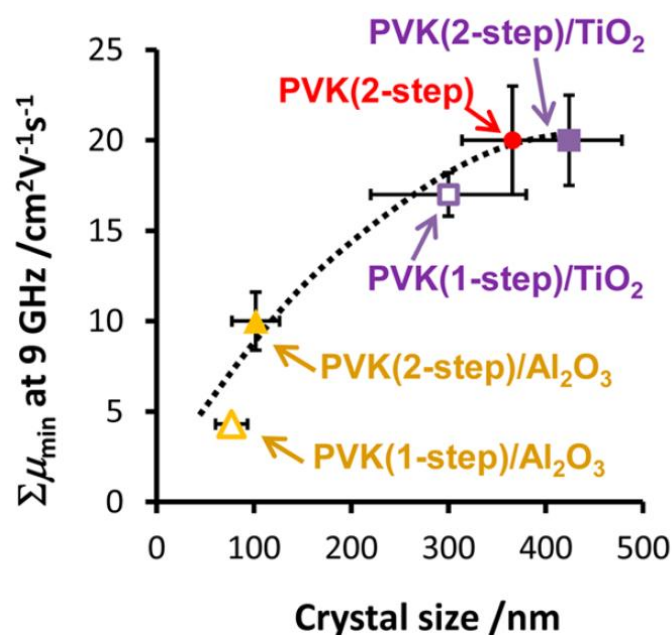


Fig. 18. Plot of $\Sigma\mu_{\min}$ measured by time-resolved microwave conductivity at 9 GHz (Table 1) versus averaged crystal size. Reproduced with permission from (Oga et al., 2014).

To obtain a more complete analysis of the energetic profile and especially close to the contacts one needs to take into account ionic conductivity effects previously discussed in Fig. 8. Therefore, extraction of photogenerated carriers at the contacts may be limited in many cases by the energy level profile but it can also be limited by the chemical reactivity of the external contact with the perovskite material. For example, during cycling of the device under dark conditions reversible generation of Ti-I-Pb bonds have been reported to take place at the interface between the perovskite materials and TiO_2 (Carrillo et al., 2016) and this will be discussed in detail in section 7. Depending on the external contact this type of reactivity could generate insulating species that pose a source for series resistance to the device.

Using KPFM microscopy (Bergmann et al., 2014) studied the contact potential difference profile of devices containing mesoporous TiO_2 layer under different illumination conditions. It was observed that the electrical field distribution across the devices depends markedly on the illumination conditions, see Fig. 19. The authors showed that under dark conditions the potential drop in the mesoporous TiO_2 /perovskite layer was homogenous. Alternatively, in the capping perovskite layer the electrical field was rather confined to the TiO_2 . On illumination, a drastic change was observed in the capping layer being the potential drop homogeneous in the middle and the electrical field confined close to both of the external contacts TiO_2 and Spiro-OMeTAD. The authors claimed that on illumination holes accumulate in front of the hole-transport layer as a consequence of unbalanced charge transport in the device. However, at the time it was not known about the ionic transport to the external contacts so ion accumulation at

the contacts could well be responsible for such a behavior. Importantly, after light illumination some permanent changes (within the timescale of the measurement) were observed which were responsible for a modification in the obtained energy level profile. This observation is more consistent with ion movements rather than hole accumulation which tend to decay quite fast.

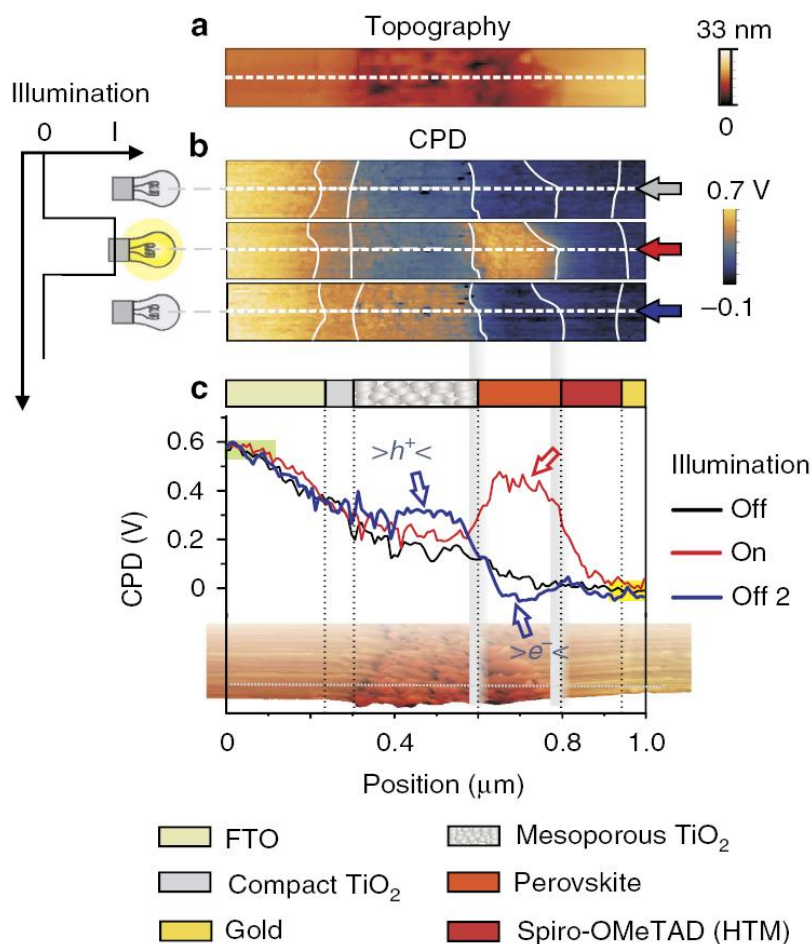


Fig. 19. Comparison of representative KPFM results of a device containing mesoporous TiO₂ measured under dark and light conditions under short-circuit conditions. As can be observed CPD line profiles are different before illumination, during illumination and immediately after illumination. Reprinted from (Bergmann et al., 2014).

6. Transient photovoltage and photocurrent

Time transient experiments that probe the decay of electrical or optical properties are widely used to obtain the properties of charge generation, recombination and the fundamental mechanisms of voltage and current generation in hybrid organic-inorganic solar cells as dye-sensitized solar cells and organic solar cells (Clifford et al., 2012). These transient decays consist of the measurement of the response to a step change.

Depending on the perturbation several methods are distinguished. Open-circuit voltage decay (OCVD) (Zaban et al., 2003) is a large perturbation method in which illumination is removed and the decay of photovoltage is monitored. Transient Photovoltage Decays (TPD) consists of the decay of a small perturbation step of illumination, again monitoring a photovoltage, while in Transient Absorption Spectroscopy (TAS), the optical absorption properties are probed.

6.1. Open-circuit voltage decay

The method of OCVD has been widely used to determine electron lifetime in dye-sensitized solar cells, which is obtained directly by a reciprocal derivative of the voltage (Zaban et al., 2003). However, the interpretation of decays in hybrid halide perovskite appears to require a very different framework concerning the physical origin of the decay (Bertoluzzi et al., 2015). Time transient decays in perovskite solar cells span a very complex phenomenology and the model required to extract decay times are often uncertain, ranging from multiple exponentials to stretched exponential (Roiati et al., 2014, Listorti et al., 2015). A slow response associated to recovery of the dark polarization in perovskite solar cells (Baumann et al., 2014, Sanchez et al., 2014) should be connected to the observations made by capacitance spectroscopy and voltage sweep methods, that indicate a dominance of complex ionic-electronic relaxation phenomena at the external interfaces of the device. In addition there are faster component which can be related to the observations by small perturbation TPD (Lee et al., 2014, Roiati et al., 2014, Stranks et al., 2014).

Since the slow decay of OCVD cannot be attributed directly to recombination, and in addition other fast decay components are observed in the transient of photovoltage, we have defined (Bertoluzzi et al., 2015) an *instantaneous relaxation time* τ_{ir} that describes a general relaxation phenomenon by the following expression

$$\frac{dV}{dt} = -\frac{1}{\tau_{ir}} V \quad (9)$$

The characteristic time τ_{ir} is a constant only if the voltage decay obeys an ideal relaxation exponential law. Otherwise τ_{ir} is a function of the voltage that can be generally determined as

$$\tau_{ir}(V) = \left(-\frac{1}{V} \frac{dV}{dt} \right)^{-1} \quad (10)$$

The time $\tau_{ir}(V)$ describes the instantaneous advance of the relaxation, being different from the (Zaban et al., 2003) definition that applies for a recombination lifetime.

The representation of $\tau_{ir}(V)$ let us discriminate the different types of relaxation dynamics. In Fig. 6c decays of devices with different hole extraction contacts are shown with nearly constant decay time. Interestingly, the relaxation time is much shorter for the sample that has the smaller capacitance (Fig. 6d), as previously discussed. In

contrast to this, samples with mesoporous electrodes show more complex long time decay characteristics as indicated in Fig. 20. Fig. 21 shows that a modification of the oxide contact modifies the instantaneous relaxation time of the voltage decay.

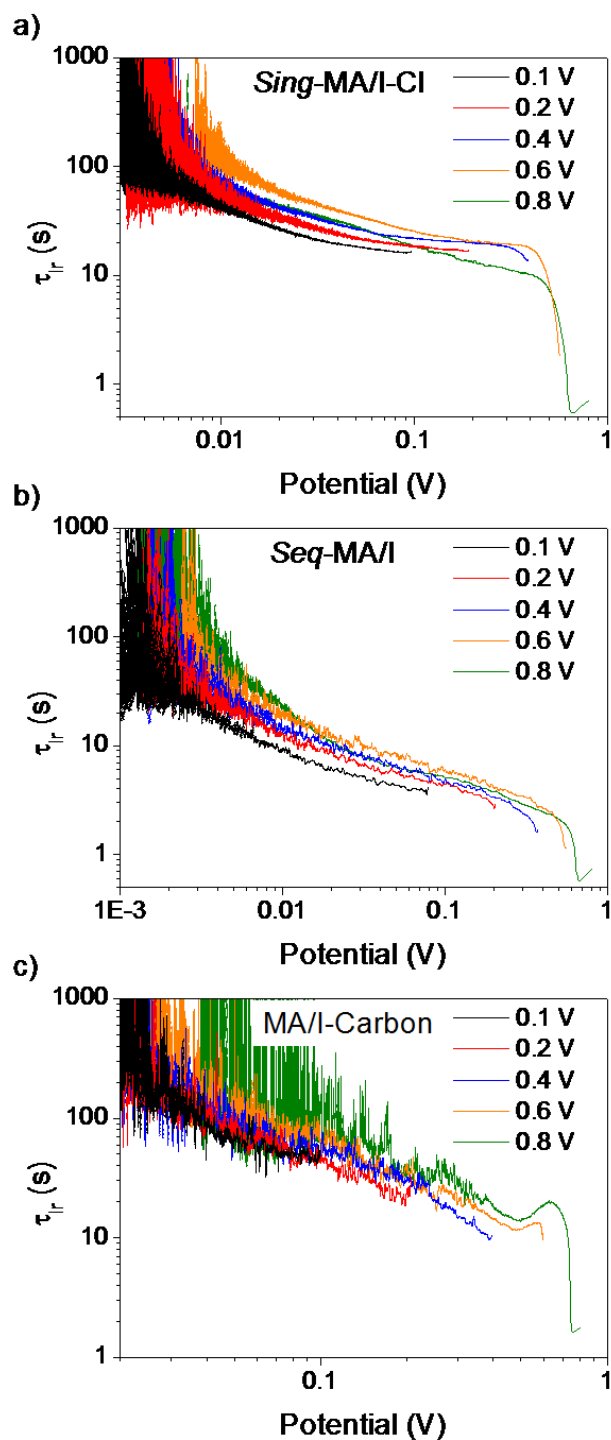


Fig. 20. Instantaneous relaxation time as function of voltage for three different $\text{CH}_3\text{NH}_3\text{PbI}_{3-x}\text{Cl}_x$ perovskite solar cells. The starting value of voltage is indicated for each cell. (a) *Sing-MA/I-Cl* is formed by single step deposition, using PbCl_2 precursor,

of $\text{CH}_3\text{NH}_3\text{PbI}_{3-x}\text{Cl}_x$ onto a compact $\text{TiO}_2/\text{meso-TiO}_2$ electrode and using Spiro-MeOTAD as hole contact. (b) *Seq-MA/I* were prepared by exploiting the sequential methodology, which consists on depositing by spin-coating a layer of PbI_2 onto a compact $\text{TiO}_2/\text{meso-TiO}_2$ electrode, followed by the addition of a $\text{CH}_3\text{NH}_3\text{I}$ solution to form the $\text{CH}_3\text{NH}_3\text{PbI}_3$ and using Spiro-MeOTAD as hole contact. These two methods, configuration and materials are probably the most extended in the current literature of PSCs. (c) MA/I-Carbon. The third configuration of devices consist on the deposition of $\text{CH}_3\text{NH}_3\text{PbI}_3$ by drop casting onto a $\text{meso-TiO}_2/\text{meso-ZrO}_2/\text{Carbon}$ electrode, thus consisting on a hole conductor-free device. Reprinted from (Bertoluzzi et al., 2015).

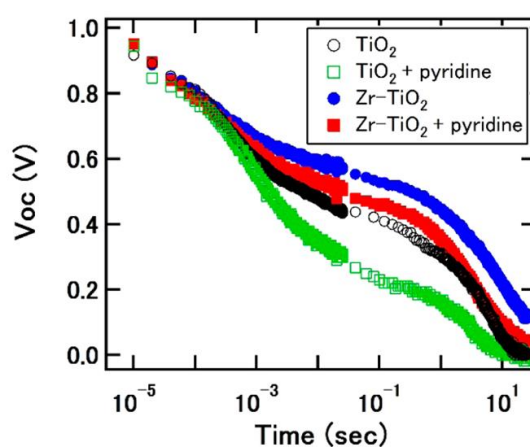


Fig. 21. Open-circuit voltage transients for the four different perovskite device types FTO/Zr-TiO₂ (or TiO₂)/CH₃NH₃PbI₃(Cl)/*spiro*-OMeTAD/Au. The oxide contact has different compositions as indicated in the figure legends. Reprinted from (Nagaoka et al., 2015).

6.2. Transient current and charging

As discussed in previous sections, accumulation of ionic species in the vicinity of the contact brings about electrode polarization and concomitant capacitive responses. The long time decays observed in Fig. 20 indicate a complex slow relaxation but so far it has not been identified in terms of a physical process. An alternative way of analyzing ionic charging is by measuring *charge* transients instead of current transients as in Fig. 1a. The advantage of this method from the experimental point of view is that charge yields a growing response as a function of time, while current decreases below usual detection limits. An example of the charge response to a voltage step is depicted in Fig. 22. Thick $\text{CH}_3\text{NH}_3\text{PbI}_3$ samples sandwiched between inert Au electrodes exhibit double exponential charging shapes with typical response time of order 10 s for the slowest component (Fig. 22b) (Almora et al., 2016). An analysis of these transients provides important information on the ultraslow relaxation of perovskite solar cells.

Charging profiles reveal the structure of the ionic double-layer made up of Helmholtz layer at $\text{MAPbI}_3/\text{contact}$ interface and electrode-induced local charge imbalance within

the ion diffuse layer, as outline in Fig. 8b. Ionic accumulation within the diffuse layer is well described by Eq. (6).

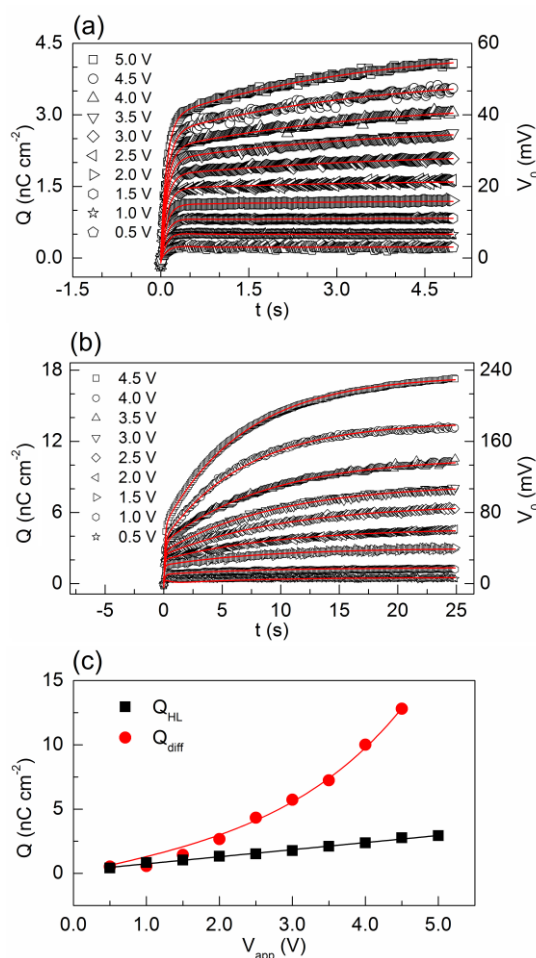


Fig. 22. Example of Q (and V_0) signals of an 800 μm -thick MAPbI_3 pellet sandwiched between Au contacts for short (a) and long (b) measuring times. (c) Values of Q_{HL} (Helmholtz layer) showing a linear trend (solid line) in accordance to a plane capacitor behavior. Ionic charge Q_{diff} (diffuse layer) values following fitting of Equation 8 (solid line). Reprinted from (Almora et al., 2016).

Based on this interpretation associated to the Gouy-Chapman layer it is proposed that ionic charging, with a typical response time of 10 s, is a local effect confined in the vicinity of the electrode (with extent $L_D \ll L$). This observation entails steady-state ionic space charge of ~ 10 nm-width at the contacts from Eq. (7) using $N \approx 10^{17} \text{ cm}^{-3}$, in contrast to other approaches that suggest non-negligible net mobile ionic concentration entering the perovskite bulk. For example the chronoamperometric transient signal obtained upon illumination (Fig. 23) using much shorter perovskite layer thickness (500 nm), has been interpreted in relation of ionic rearrangement in the entire absorber size (Bag et al., 2015, Eames et al., 2015). Both models predict ion accumulation of different

extent that produces partial screening of the electrical field within the perovskite film. Also much longer voltage transients measured with thicker (0.6 mm) samples have been interpreted as resulting from ion movement (Fig. 9) (Yang et al., 2015).

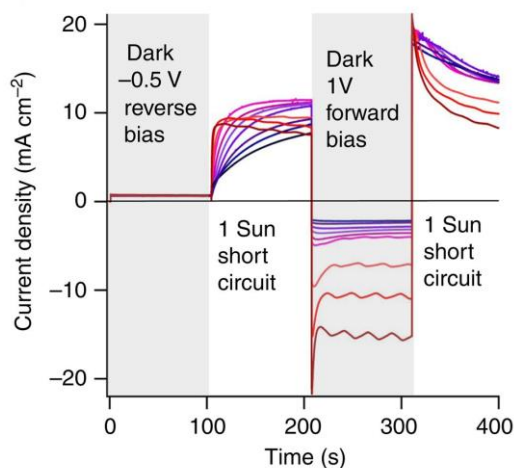


Fig. 23. Chronophotoamperometry measurements of a perovskite based cell. The measurement sequence in a $d\text{-TiO}_2/\text{CH}_3\text{NH}_3\text{PbI}_3/\text{spiro-OMeTAD}/\text{Au}$ cell is indicated; measured temperatures (to the nearest 0.5 °C) of the devices were -9.5 (dark blue), -5.5, 0.5, 5, 10.5, 15, 19.5, 24.5, 30, 40 and 50 °C (dark red). Reprinted from (Eames et al., 2015).

6.3. Small perturbation illumination methods: Transient photovoltage and charge extraction.

Photo-induced time resolved techniques such as charge extraction (CE) and TPV have been widely employed in the field of dye-sensitized solar cells and organic solar cells to determine capacitances and lifetimes. The results have been found in excellent correlation with those of impedance spectroscopy, which provides a coherent and robust picture of dynamic carrier phenomena in these systems (Etxebarria et al., 2014). The key issue when employing CE instead of IS is that the CE decay must be much faster than the TPV decay under 1 sun illumination conditions. The solar cell charge density can be also measured using differential charging, a method that combines the use of TPV and Transient Photocurrent (TPC), with identical results to either IS or CE in devices measured previously as organic or sensitized solar cells.

However, substantial differences between the results of these methods have been found in measurements of lead halide perovskite solar cells, either using mesoporous TiO_2 or not as scaffold, which respect to the former classes of devices. In contrast to the previous systems in the perovskite solar cells, the CE decay results much longer than the TPV decay (Marin-Beloqui et al., 2016), Fig. 24. In addition the measured charge density when using differential charging is different to the results obtained by CE as shown in Fig. 25.

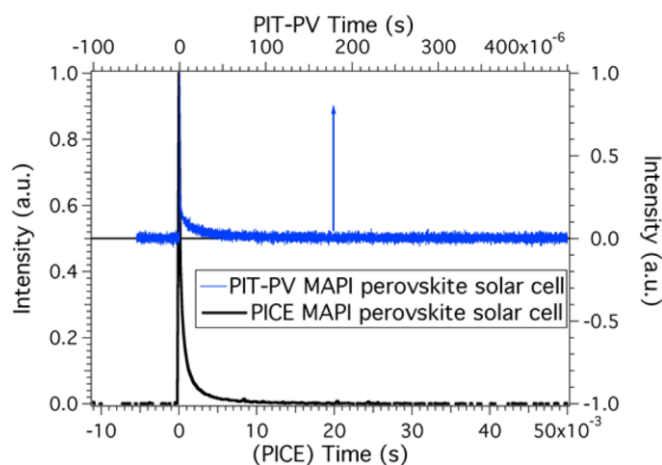


Figure 24. Top, charge extraction decay at 1 sun for a 12.7% efficient lead perovskite solar cell. Bottom, TPV decay at the same light intensity (1 sun) for the same solar cell. Reprinted from (Marin-Belouqui et al., 2016).

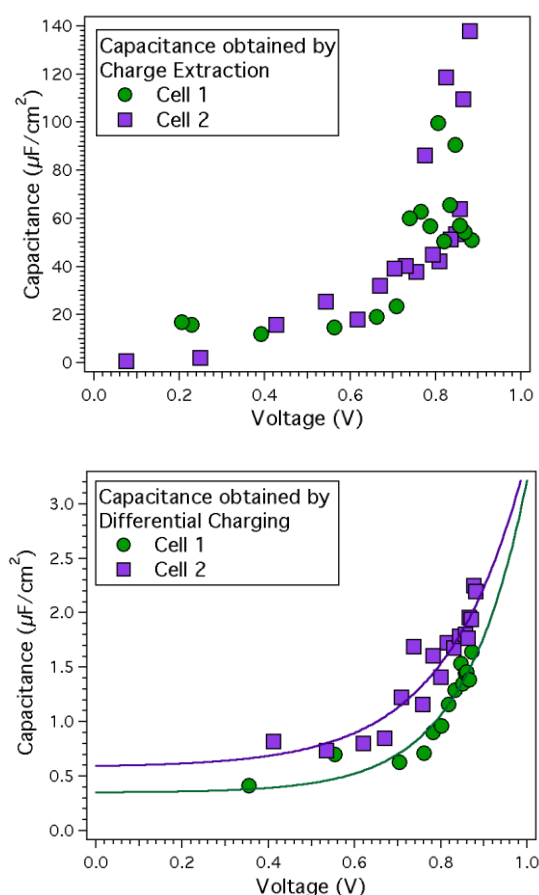


Figure 25. Top, solar cell charge density at different light bias measured using charge extraction. Bottom, solar cell charge density measured at different light bias using differential charging. Data courtesy of Emilio Palomares (ICIQ).

The main difference between both techniques, CE and differential charging, is the acquisition time. The differential charging method let obtain the cell capacitance through the expression

$$C(V_{oc}) = \frac{dQ}{dt} \left(\frac{dV}{dt} \right)^{-1} \quad (11)$$

The dV/dt is obtained directly from the TPV transients at different light bias and the dQ/dt is measured using TPC. The TPC decay under different light intensities reaches a plateau that can be taken as the maximum charge generation flux. The TPC is the voltage response of a solar cell but measured at short circuit using the same laser pulse as that used for the TPV. The TPC decay is converted into a current transient using a small resistor (typically 40-50 Ω) and applying Ohm's law. Yet, this assumption is only valid if (a) there are not critical charge losses at short-circuit (basically meaning that the device J_{sc} is linear when increasing the light intensity); (b) the dQ does not change substantially under different light illumination conditions and (c) the TPV decay is slower than the TPC (meaning that charge collection is much faster than charge recombination). Despite the uncertainties associated to the interpretation of this technique (which is common to other transient methods as mentioned before), according to the initial suggestion of (O'Regan et al., 2015) the measured charge using differential charging is associated to a given carrier lifetime which can be used to reproduce, within the experimental error, the solar cell photocurrent at a given light bias.

7. Reactivity and degradation at electrodes

The property of ionic charging by ionic vacancy or interstitial migration and subsequent accumulation at the outer boundaries of the perovskite layer, has already been commented extensively. Ionic charging may provide complex experimental characterizations, particularly if contacts cannot be considered as blocking electrodes, i.e., when Faradaic currents (non-blocking or reacting electrodes) or high applied voltages may yield large extent space-charge regions entering the layer bulk (Bazant et al., 2004). In these cases the interface polarization is dominated by the complex interaction between electronic and ionic species at both sides of the contact (Mariappan et al., 2010, Kato et al., 2015) instead of simple Debye capacitances of Eq. (8). Reactivity at the interfaces between the perovskite film and the electron- or hole-transporting contact materials is then an issue of primary concern.

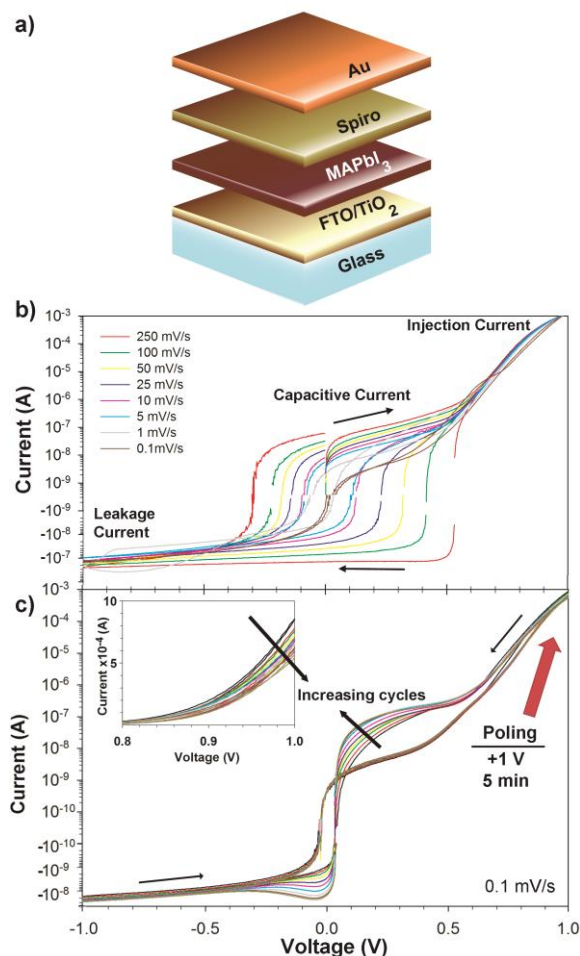


Fig. 26. (a) Structure of the planar solar cells (200 nm MAPbI₃ layer). (b) Dark currents measured at different scan rates both for positive and negative sweep. Three different mechanisms are identified: at $V > 0.5$ V operation currents caused by carrier injection, $V < -0.5$ V leakage currents, and central voltage interval shows the presence of scan-rate dependent, capacitive currents. (c) Cycled experiments including positive poling during 5 min. Positive scan (no poling) reproduce steady-state behavior. Negative scans induce incremental redox peaks after successive cycles. In the inset: injection current at forward bias decreases with cycling. Reprinted from (Carrillo et al., 2016).

Recent experiments performed on complete solar cells of planar structure FTO/TiO₂/MAPbI₃/spiro-OMeTAD/Au (Fig. 26a), and symmetrical FTO/TiO₂/MAPbI₃/TiO₂/FTO and Au/spiro-OMeTAD/MAPbI₃/spiro-OMeTAD/Au devices (Fig. 26d-e) have enabled progress in the role of interfaces on the capacitive hysteresis and solar cell degradation (Carrillo et al., 2016). Two separate types of reactivity sources (reversible and irreversible) have been identified:

(i) The formation of weak Ti–I–Pb bonds at the TiO₂/MAPbI₃ interface that facilitate interfacial accommodation of moving iodine ions. This interaction produces highly reversible capacitive currents (Fig. 26b), without altering steady-state photovoltaic

features. As observed in the central voltage window of Fig. 26b, capacitive currents exhibit the expected square-like response previously described in Fig. 3.

(ii) Chemical reaction between *spiro*-OMeTAD⁺ and moving I⁻ which progressively reduces the hole transporting material conductivity and deteriorates solar cell performance. This reaction results in an irreversible redox peak only observable after positive poling at slow scan rates (Fig. 26c).

These results highlight the key role that interlayers used as selective contacts play on perovskite solar cell stability, in addition to the intrinsic reactivity of the perovskite materials (Conings et al., 2015). As an example of the dramatic effect of the contact layers it is shown in Fig. 27 the performance of inverted type architectures (Fig. 2c) using oxide and organic compounds. It is evident that oxide layers (NiO_x and ZnO) improve the solar cell stability by protecting it against intrinsic, oxygen and water reactivity (You et al., 2016).

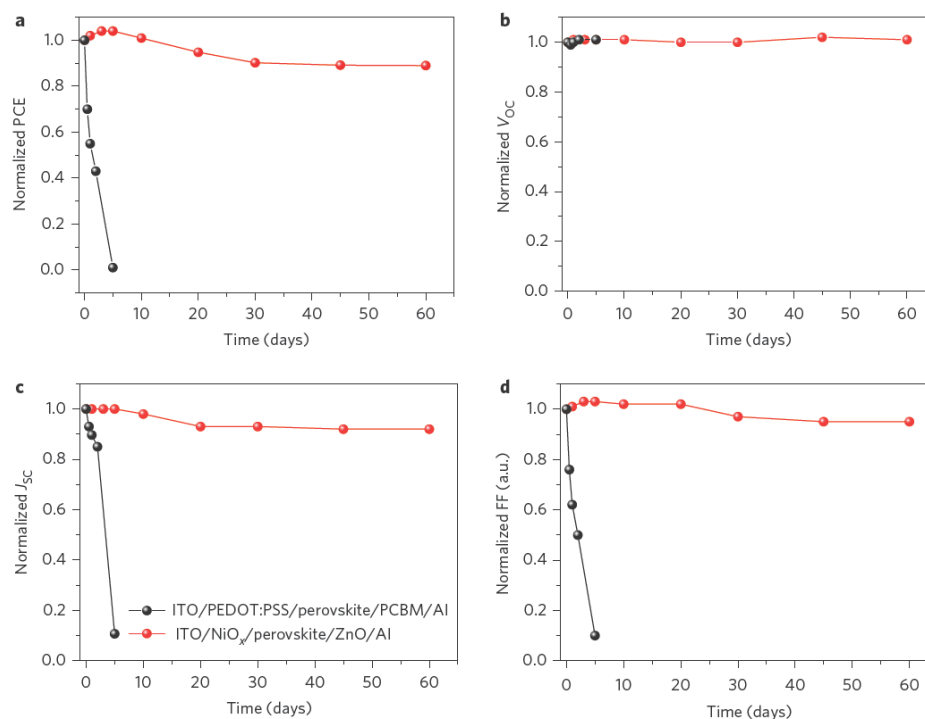


Fig. 27. Stability of the devices in an ambient environment without encapsulation. Device performances of ITO/PEDOT:PSS/perovskite/PCBM/Al (black) and ITO/NiO_x/perovskite/ZnO/Al (red) structures as a function of storage time in an ambient environment (30–50% humidity, T=25 °C). Reprinted from (You et al., 2016).

Degradation of a series of devices in the configuration ITO/PEDOT:PSS/Perovskite/PCBM/Metal has recently been studied using a range of different top metals (Guerrero et al., 2015). Degradation readily occurred after illumination in the glovebox during 2 hours obtaining S-shape *J-V* curves for devices prepared with either Ca, Al, Ag or Au. Different techniques were used to understand the

degradation processes and all pointed to interfacial degradation which was introducing a source of series resistance that was promoting interfacial recombination processes. In particular, devices showing an S-shape measured in the dark after degradation did not change significantly the doping density indicating that the bulk properties of the devices had not significantly changed. More intriguing was the fact that the V_{fb} shifted towards negative values for degraded sample indicating that the interface equilibration with the perovskite semiconductor was being modified, see Fig. 18. Measurements under light conditions further shifted V_{fb} towards negative values pointing to generation of light induced dipoles at perovskite/contact interface. Alternatively, a top metal based on $\text{Cr}_2\text{O}_3/\text{Cr}$ enhanced the stability against corrosion and no S-shape was observed. Results from C - V did not show significant shifts in V_{fb} for fresh and degraded devices either in the dark or light and the most relevant result was a moderate increase in the doping density of the perovskite layer for degraded device.

Trap-induced degradation of perovskite solar cells has recently been reported where a large density of hole traps is formed by continuous solar illumination strongly limiting the device stability (Qin et al., 2016). In the experiment devices in the configuration ITO/PEDOT:PSS/Perovskite/ PC_{70}BM /LiF/Al are prepared. Processing of the perovskite layer takes place either in air or nitrogen and initial efficiencies are very similar. Whilst efficiencies of devices prepared in nitrogen environment only decay about 10 % during the first 500 h devices fabricated in air reduce the efficiency up to 90% in the same period of time. To investigate the degradation origin the carrier traps were analyzed using the thermally stimulated current (TSC) measurement. In this technique, carrier traps in a cooled device at 77 K are filled with carriers injected from the electrodes under a small forward bias. By gradually increasing the temperature at a constant rate under a small reverse bias the trapped carriers are then released and collected. Fig. 28 displays the TSC curves of device fabricated in air before and after degradation by 500 h of illumination. Whilst fresh device does not show any peak in the TSC curve two peaks are clearly observed at temperature of 161K and 213 K for the degraded device originated from the release of carriers from the trap sites. Hole-trap depths of 0.32 and 0.42 eV are calculated from the low and high-temperature TSC, respectively. Generation of these trap states acts as a recombination center reducing the device efficiency. The authors concluded that water molecules included in the $\text{CH}_3\text{NH}_3\text{PbI}_3$ layer were responsible for both TSC signals. However, the precise mechanism in which these traps are generated is still unclear and could indeed be a case of reactivity at the contacts.

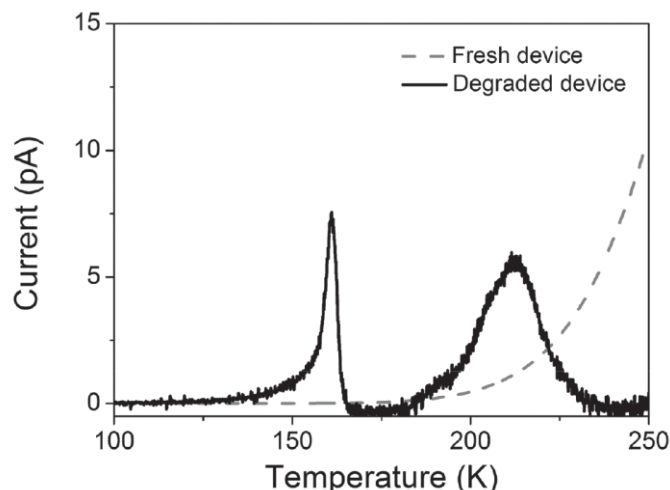


Fig. 28: TSC curves of devices in the configuration ITO/PEDOT:PSS/Perovskite/PC₇₀BM/LiF/Al fabricated in air before and after degradation by 500 h of illumination. Reprinted from (Qin et al., 2016).

8. The light capacitances

As commented before in Fig. 12 and Fig. 14, under illumination the low frequency capacitances in perovskite solar cells undergo a very large increase, that is observed to depend linearly on illumination (Juarez-Perez et al., 2014). Since measurements of a number of cells have been independently reported (Yang et al., 2015, Li et al., 2016, Zarazua et al., 2016), the photoinduced capacitance is established as a normal property of lead halide perovskite solar cells. The measurements indicate that this property occurs irrespective of type of contacts (symmetric, asymmetric, nanoporous...), however the specific features are dramatically changed by contacts as is evident in Fig. 11, which shows a connection between low frequency capacitance and amount of hysteresis (Kim et al., 2015).

Different explanations have been presented in the literature to rationalize the photoinduced giant capacitance at low frequency: (a) A change of electrode polarization capacitance. This will be associated to an increasing concentration of mobile ions, caused by the excess electronic carriers. (b) A change of the bulk polarizability. In this model there occurs an enhancement of the elementary dipole in the perovskite octahedral cage caused by light generated carriers (Wu et al., 2014). (c) A change of the chemical capacitance, homogeneously in the bulk perovskite layer (Yang et al., 2015).

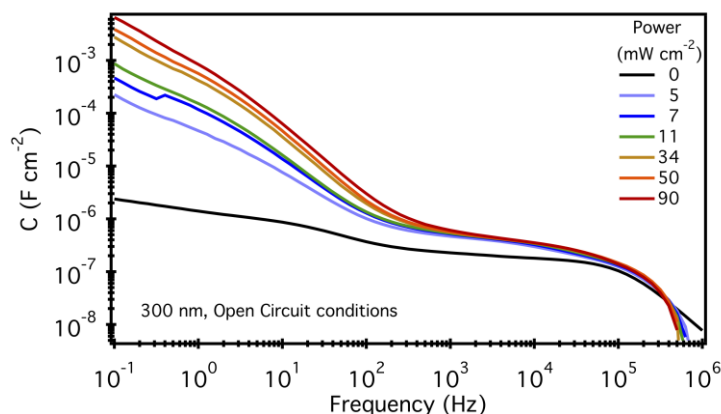


Fig. 29. Capacitance spectra measured in open-circuit conditions for different illumination intensities of 300 nm-thick solar cells of structure FTO/TiO₂/FAPbI_{3-x}Cl_x/spiro-OMeTAD/Au, where FA is CH(NH₂)₂ between 100 mHz and 1 MHz. Dark response at zero-bias is also shown. Reprinted from (Zarazua et al., 2016).

As commented above, recent measurements using a variety of methods such as voltage cycling and capacitance spectroscopy point out that the low frequency capacitance in the dark is associated to ionic pile up at the interface (Almora et al., 2015). However, a large rise of the total measured capacitance is prevented by any series capacitor. In the case of ionic space charge, capacitance is limited by the Helmholtz capacitance situated in series, so that one does not expect values substantially higher than $\mu\text{F cm}^{-2}$. The low-frequency capacitance increase observed in Fig. 29 greatly exceeds the mentioned Helmholtz capacitance limit, so that it is unlikely that this large capacitance can be interpreted in terms of the diffuse ionic double layer. Therefore it is reasonable to assume a parallel pathway in which *electronic* photogenerated carriers form a large interfacial capacitance. (Li et al., 2016) assumed that the enhancement of capacitance originates from native defects and their accompanied defect dipoles which need to be activated by photogenerated charge carriers.

Another type of electronic interfacial effect has been suggested by (Zarazua et al., 2016) that is supported by some experimental evidence. At semiconductor surfaces, very large electronic interfacial capacitance is possible in the domains of accumulation and inversion, as there is no limit to the packing of electrons in a short distance at the vicinity of the contact.

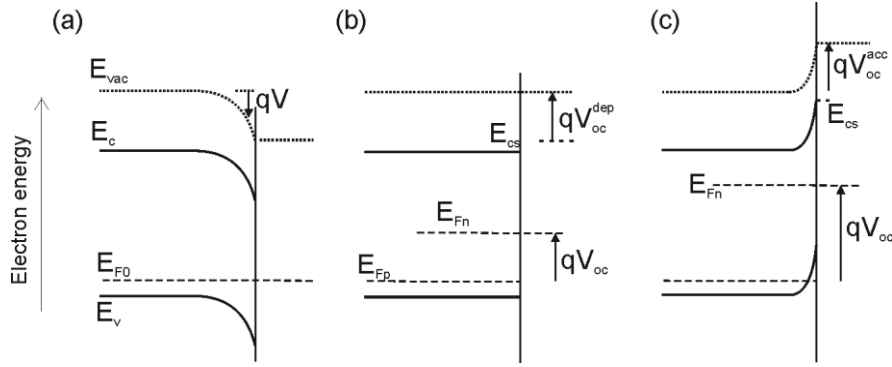


Fig. 30. Energy diagram for electron selective contact to the semiconductor absorber layer at open circuit conditions. (a) Depletion layer at equilibrium. Generation of minority carriers produces flatband condition (b) and further accumulation (c) of majority carrier. The total open circuit voltage is the increase of minority carrier Fermi level that corresponds to total change of surface vacuum level as $V_{oc} = V_{oc}^{dep} + V_{oc}^{acc}$. Reprinted from (Zarazua et al., 2016).

Taking for example the p -type semiconductor surface, the conduction band bends upward at the surface and penetrates the Fermi level, as shown in Fig. 30. The charge per unit surface is $Q = qp_b L_D F_s$ (Mönch, 1993), where p_b is the bulk carrier density corresponding to dopant density, $F_s \approx \sqrt{2} e^{qV/2k_B T}$, where qV corresponds to local separation of vacuum level (VL) from bulk value. The Debye length is given in Eq. (7). For the capacitance we find the standard expression

$$C_s = \frac{dQ}{dV} = \frac{qp_b^{1/2}}{\sqrt{2}} \left(\frac{\epsilon_r \epsilon_0}{k_B T} \right)^{1/2} e^{qV/2k_B T} \quad (12)$$

Accumulation capacitance is in fact very common in transistor and metal-insulator-semiconductor devices (Sze, 1981), although the measured capacitance is limited by the series connection of the oxide dielectric capacitance. In a perovskite solar cell, the accumulation region will be connected by two conducting regions (perovskite and oxide semiconductor), so that in principle it can take very large values. (Zarazua et al., 2016) It was reported that low-frequency capacitance values increase proportionally with the light intensity, and are also proportional to the perovskite layer thickness. The observation of these two proportionalities (light intensity and film thickness) constitutes a direct proof that the surface capacitance charging is made up of photogenerated carriers coming from the absorber bulk. In addition the capacitance dependence on voltage shows the characteristic slope of $1/2k_B T$ for solar cells with different absorber perovskite thickness, in agreement with the accumulation capacitance expression (12).

Conclusion

The analysis of perovskite solar cells using impedance spectroscopy, time transient decays, and voltage cycling, shows that the phenomenology is extremely varied and complex but nonetheless it is possible to identify some trends of the equivalent circuit

elements of the solar cell devices. There is a large impact of ionic accumulation at the interface in the low frequency response, and furthermore the ionic transport produces temporary and even permanent modifications of the interface of the perovskite with charge extraction layers, that cause phenomena as hysteresis and degradation. Capacitances at high frequency indicate bulk relaxation phenomena but under applied bias they can be related to a depletion capacitance. A widely reported observation of very low frequency capacitance with illumination has been attributed to electronic accumulation capacitance at the perovskite/contact interface. It is stressed then that hysteresis effects are originated by local charging at the contacts, either ionic as observed in dark responses (Fig. 15), or electronic through the formation of light-induced accumulation zones (Fig. 29). These mechanisms are both largely confined within a short extent near the contacts (~10 nm) introducing a local modification of the electrical field. These observations pave the way for a fuller understanding of dynamic characteristics of perovskite solar cell that will require insight about the meaning of resistances.

References

- Almora, O.; Guerrero, A.; Garcia-Belmonte, G. "Ionic charging by local imbalance at interfaces in hybrid lead halide perovskites". *Applied Physics Letters* **2016**, DOI: 10.1063/1061.4941033.
- Almora, O.; Zarazua, I.; Mas-Marza, E.; Mora-Sero, I.; Bisquert, J.; Garcia-Belmonte, G. "Capacitive dark currents, hysteresis, and electrode polarization in lead halide perovskite solar cells". *The Journal of Physical Chemistry Letters* **2015**, *6*, 1645-1652.
- Azpiroz, J. M.; Mosconi, E.; Bisquert, J.; De Angelis, F. "Defect migration in methylammonium lead iodide and its role in perovskite solar cell operation". *Energy & Environmental Science* **2015**, *8*, 2118-2127.
- Bag, M.; Renna, L. A.; Adhikari, R. Y.; Karak, S.; Liu, F.; Lahti, P. M.; Russell, T. P.; Tuominen, M. T.; Venkataraman, D. "Kinetics of ion transport in perovskite active layers and its implications for active layer stability". *Journal of the American Chemical Society* **2015**, *137*, 13130-13137.
- Baumann, A.; Tvingstedt, K.; Heiber, M. C.; Vath, S.; Momblona, C.; Bolink, H. J.; Dyakonov, V. "Persistent photovoltage in methylammonium lead iodide perovskite solar cells". *APL Materials* **2014**, *2*, 081501.
- Bazant, M. Z.; Thornton, K.; Ajdari, A. "Diffuse-charge dynamics in electrochemical systems". *Physical Review E* **2004**, *70*, 021506.
- Beaumont, J. H.; Jacobs, P. W. M. "Polarization in potassium chloride crystals". *Journal of Physical Chemistry of Solids* **1967**, *28*, 657.
- Bergmann, V. W.; Weber, S. A. L.; Javier Ramos, F.; Nazeeruddin, M. K.; Gratzel, M.; Li, D.; Domanski, A. L.; Lieberwirth, I.; Ahmad, S.; Berger, R. "Real-space observation of unbalanced charge distribution inside a perovskite-sensitized solar cell". *Nat Commun* **2014**, *5*.
- Bertoluzzi, L.; Sanchez, R. S.; Liu, L.; Lee, J.-W.; Mas-Marza, E.; Han, H.; Park, N.-G.; Mora-Sero, I.; Bisquert, J. "Cooperative kinetics of depolarization in CH₃NH₃PbI₃ perovskite solar cells". *Energy & Environmental Science* **2015**, *8*, 910-915.
- Bisquert, J.; Fabregat-Santiago, F. in *Dye-sensitized solar cells.*; Kalyanasundaram, K., Ed.; CRC Press: Boca Raton, 2010.
- Bisquert, J.; Garcia-Belmonte, G.; Mora-Sero, I. in *Unconventional Thin Film Photovoltaics: Organic and Perovskite Solar Cells*; Como, E. d., Angelis, F. D., Snaith, H., Walker, A., Eds.; RSC Energy and Environment Series, 2016.
- Brivio, F.; Butler, K. T.; Walsh, A.; van Schilfgaarde, M. "Relativistic quasiparticle self-consistent electronic structure of hybrid halide perovskite photovoltaic absorbers".

Physical Review B **2014**, *89*, 155204.

Brivio, F.; Walker, A. B.; Walsh, A. "Structural and Electronic Properties of Hybrid Perovskites for High-Efficiency Thin-Film Photovoltaics from First-Principles". *APL Materials* **2013**, *1*, 042113.

Carrillo, J.; Guerrero, A.; Rahimnejad, S.; Almora, O.; Zarazua, I.; Mas-Marza, E.; Bisquert, J.; Garcia-Belmonte, G. "Ionic reactivity at contacts and aging of methylammonium lead triiodide perovskite solar cell ". *Advanced Energy Materials* **2016**.

Chen, B.; Yang, M.; Zheng, X.; Wu, C.; Li, W.; Yan, Y.; Bisquert, J.; Garcia-Belmonte, G.; Zhu, K.; Priya, S. "Impact of capacitive effect and ion migration on the hysteretic behavior of perovskite solar cells". *The Journal of Physical Chemistry Letters* **2015**, *6*, 4693–4700.

Chih-Tang, S.; Noyce, R. N.; Shockley, W. "Carrier Generation and Recombination in P-N Junctions and P-N Junction Characteristics". *Proceedings of the IRE* **1957**, *45*, 1228-1243.

Clifford, J. N.; Martinez-Ferrero, E.; Palomares, E. "Dye mediated charge recombination dynamics in nanocrystalline TiO₂ dye sensitized solar cells". *Journal of Materials Chemistry* **2012**, *22*, 12415-12422.

Coll, M.; Gomez, A.; Mas-Marza, E.; Almora, O.; Garcia-Belmonte, G.; Campoy-Quiles, M.; Bisquert, J. "Polarization Switching and Light-Enhanced Piezoelectricity in Lead Halide Perovskites". *The Journal of Physical Chemistry Letters* **2015**, 1408-1413.

Conings, B.; Drijkoningen, J.; Gauquelin, N.; Babayigit, A.; D'Haen, J.; D'Olieslaeger, L.; Ethirajan, A.; Verbeeck, J.; Manca, J.; Mosconi, E.; De Angelis, F.; Boyen, H.-G. "Intrinsic Thermal Instability of Methylammonium Lead Trihalide Perovskite". *Advanced Energy Materials* **2015**, *5*, 1500477.

Eames, C.; Frost, J. M.; Barnes, P. R. F.; O'Regan, B. C.; Walsh, A.; Islam, M. S. "Ionic transport in hybrid lead iodide perovskite solar cells". *Nat Commun* **2015**, *6*.

Etxebarria, I.; Guerrero, A.; Albero, J.; Garcia-Belmonte, G.; Palomares, E.; Pacios, R. "Inverted vs standard PTB7:PC70BM organic photovoltaic devices. The benefit of highly selective and extracting contacts in device performance". *Organic Electronics* **2014**, *15*, 2756-2762.

Fabregat-Santiago, F.; Garcia-Belmonte, G.; Mora-Seró, I.; Bisquert, J. "Characterization of nanostructured hybrid and organic solar cells by impedance spectroscopy". *Physical Chemistry Chemical Physics* **2011**, *13*, 9083–9118.

Fabregat-Santiago, F.; Mora-Seró, I.; Garcia-Belmonte, G.; Bisquert, J. "Cyclic voltammetry studies of nanoporous semiconductor electrodes. Models and application to nanocrystalline TiO₂ in aqueous electrolyte". *The Journal of Physical Chemistry B*

2003, *107*, 758-769.

Fan, Z.; Xiao, J.; Sun, K.; Chen, L.; Hu, Y.; Ouyang, J.; Ong, K. P.; Zeng, K.; Wang, J. "Ferroelectricity of CH₃NH₃PbI₃ Perovskite". *The Journal of Physical Chemistry Letters* **2015**, *6*, 1155-1161.

Filippetti, A.; Delugas, P.; Saba, M. I.; Mattoni, A. "Entropy-Suppressed Ferroelectricity in Hybrid Lead-Iodide Perovskites". *The Journal of Physical Chemistry Letters* **2015**, *6*, 4909-4915.

Frost, J. M.; Butler, K. T.; Walsh, A. "Molecular Ferroelectric Contributions to Anomalous Hysteresis in Hybrid Perovskite Solar Cells". *APL Materials* **2014**, *2*.

Gottesman, R.; Zaban, A. "Perovskites for Photovoltaics in the Spotlight: Photoinduced Physical Changes and Their Implications". *Accounts of Chemical Research* **2016**.

Guerrero, A.; Dörfling, B.; Ripolles-Sanchis, T.; Aghamohammadi, M.; Barrena, E.; Campoy-Quiles, M.; Garcia-Belmonte, G. "Interplay between Fullerene Surface Coverage and Contact Selectivity of Cathode Interfaces in Organic Solar Cells". *ACS Nano* **2013**, *7*, 4637-4646.

Guerrero, A.; Juarez-Perez, E. J.; Bisquert, J.; Mora-Sero, I.; Garcia-Belmonte, G. "Electrical field profile and doping in planar lead halide perovskite solar cells". *Applied Physics Letters* **2014**, *105*, 133902.

Guerrero, A.; Marchesi, L. F.; Boix, P. P.; Ruiz-Raga, S.; Ripolles-Sanchis, T.; Garcia-Belmonte, G.; Bisquert, J. "How the charge-neutrality level of interface states controls energy level alignment in cathode contacts of organic bulk-heterojunction solar cells". *ACS Nano* **2012**, *6*, 3453-3460.

Guerrero, A.; You, J.; Aranda, C.; Kang, Y. S.; Garcia-Belmonte, G.; Zhou, H.; Bisquert, J.; Yang, Y. "Interfacial Degradation of Planar Lead Halide Perovskite Solar Cells". *ACS nano* **2015**.

Hebb, M. H. "Electrical conductivity of silver sulfide". *The Journal of Chemical Physics* **1952**, *20*, 185.

Jiang, C.-S.; Yang, M.; Zhou, Y.; To, B.; Nanayakkara, S. U.; Luther, J. M.; Zhou, W.; Berry, J. J.; van de Lagemaat, J.; Padture, N. P.; Zhu, K.; Al-Jassim, M. M. "Carrier separation and transport in perovskite solar cells studied by nanometre-scale profiling of electrical potential". *Nat Commun* **2015**, *6*.

Juarez-Perez, E. J.; Sanchez, R. S.; Badia, L.; Garcia-Belmonte, G.; Gonzalez-Pedro, V.; Kang, Y. S.; Mora-Sero, I.; Bisquert, J. "Photoinduced giant dielectric constant in lead halide perovskite solar cells". *The Journal of Physical Chemistry Letters* **2014**, *5*, 2390-2394.

Kato, Y.; Ono, L. K.; Lee, M. V.; Wang, S.; Raga, S. R.; Qi, Y. "Silver Iodide

Formation in Methyl Ammonium Lead Iodide Perovskite Solar Cells with Silver Top Electrodes". *Advanced Materials Interfaces* **2015**, 2, 1500195.

Kim, C.; Tomozawa, M. "Electrode Polarization of Glasses". *Journal of the American Chemical Society* **1976**, 59, 127–130.

Kim, H.-S.; Jang, I.-H.; Ahn, N.; Choi, M.; Guerrero, A.; Bisquert, J.; Park, N.-G. "Control of I-V Hysteresis in CH₃NH₃PbI₃ Perovskite Solar Cell". *The Journal of Physical Chemistry Letters* **2015**, 6, 4633–4639.

Kim, H.-S.; Kim, S. K.; Kim, B. J.; Shin, K.-S.; Gupta, M. K.; Jung, H. S.; Kim, S.-W.; Park, N.-G. "Ferroelectric Polarization in CH₃NH₃PbI₃ Perovskite". *The Journal of Physical Chemistry Letters* **2015**, 6, 1729-1735.

Kim, H.-S.; Park, N.-G. "Parameters Affecting I-V Hysteresis of CH₃NH₃PbI₃ Perovskite Solar Cells: Effects of Perovskite Crystal Size and Mesoporous TiO₂ Layer". *The Journal of Physical Chemistry Letters* **2014**, 5, 2927-2934.

Kim, J.; Lee, S.-H.; Lee, J. H.; Hong, K.-H. "The Role of Intrinsic Defects in Methylammonium Lead Iodide Perovskite". *The Journal of Physical Chemistry Letters* **2014**, 5, 1312-1317.

Kirchartz, T.; Bisquert, J.; Mora-Sero, I.; Garcia-Belmonte, G. "Classification of solar cells according to mechanisms of charge separation and charge collection". *Physical Chemistry Chemical Physics* **2015**, 17, 4007-4014.

Kutes, Y.; Ye, L.; Zhou, Y.; Pang, S.; Huey, B. D.; Padture, N. P. "Direct Observation of Ferroelectric Domains in Solution-Processed CH₃NH₃PbI₃ Perovskite Thin Films". *The Journal of Physical Chemistry Letters* **2014**, 5, 3335-3339.

Lee, D.; Baek, S. H.; Kim, T. H.; Yoon, J. G.; Folkman, C. M.; Eom, C. B.; Noh, T. W. "Polarity control of carrier injection at ferroelectric/metal interfaces for electrically switchable diode and photovoltaic effects". *Physical Review B* **2011**, 84, 125305.

Lee, J.-W.; Lee, T.-Y.; Yoo, P. J.; Gratzel, M.; Mhaisalkar, S.; Park, N.-G. "Rutile TiO₂-based perovskite solar cells". *Journal of Materials Chemistry A* **2014**, 2, 9251-9259.

Leguy, A. M. A.; Frost, J. M.; McMahon, A. P.; Sakai, V. G.; Kockelmann, W.; Law, C.; Li, X.; Foglia, F.; Walsh, A.; O'Regan, B. C.; Nelson, J.; Cabral, J. T.; Barnes, P. R. F. "The dynamics of methylammonium ions in hybrid organic-inorganic perovskite solar cells". *Nat Commun* **2015**, 6.

Li, L.; Wang, F.; Wu, X.; Yu, H.; Zhou, S.; Zhao, N. "Carrier-Activated Polarization in Organometal Halide Perovskites". *The Journal of Physical Chemistry C* **2016**.

Listorti, A.; Juarez-Perez, E. J.; Frontera, C.; Roiati, V.; Garcia-Andrade, L.; Colella, S.; Rizzo, A.; Ortiz, P.; Mora-Sero, I. "Effect of Mesoporous Layer upon Crystalline Properties and Device Performance on Perovskite Solar Cells". *The Journal of Physical*

Chemistry Letters **2015**, *6*, 1628-1637.

Lunkenheimer, P.; Bobnar, V.; Pronin, A. V.; Ritus, A. I.; Volkov, A. A.; Loidl, A. "Origin of apparent colossal dielectric constants". *Physical Review B* **2002**, *66*, 052105.

Mariappan, C. R.; Heins, T. P.; Roling, B. "Electrode polarization in glassy electrolytes: Large interfacial capacitance values and indication for pseudocapacitive charge storage". *Solid State Ionics* **2010**, *181*, 859–863.

Marin-Beloqui, J. M.; Lanzetta, L.; Palomares, E. "Decreasing Charge Losses in Perovskite Solar Cells Through mp-TiO₂/MAPI Interface Engineering". *Chemistry of Materials* **2016**, *28*, 207-213.

Masaki, M.; Hattori, M.; Hotta, A.; Suzuki, I. "Dielectric Studies on CH₃NH₃PbX₃ (X= Cl or Br) Single Crystals ". *Journal of the Physical Society of Japan* **1997**, *66*, 1508-1511.

Mattoni, A.; Filippetti, A.; Saba, M. I.; Delugas, P. "Methylammonium Rotational Dynamics in Lead Halide Perovskite by Classical Molecular Dynamics: The Role of Temperature". *The Journal of Physical Chemistry C* **2015**, *119*, 17421-17428.

Mönch, W. *Semiconductor Surfaces and Interfaces*; Springer: Berlin, 1993.

Mosconi, E.; Quarti, C.; Ivanovska, T.; Ruani, G.; De Angelis, F. "Structural and electronic properties of organo-halide lead perovskites: a combined IR-spectroscopy and ab initio molecular dynamics investigation". *Physical Chemistry Chemical Physics* **2014**, *16*, 16137-16144.

Nagaoka, H.; Ma, F.; deQuilettes, D. W.; Vorpahl, S. M.; Glaz, M. S.; Colbert, A. E.; Ziffer, M. E.; Ginger, D. S. "Zr Incorporation into TiO₂ Electrodes Reduces Hysteresis and Improves Performance in Hybrid Perovskite Solar Cells while Increasing Carrier Lifetimes". *The Journal of Physical Chemistry Letters* **2015**, *6*, 669-675.

O'Regan, B. C.; Barnes, P. R. F.; Li, X.; Law, C.; Palomares, E.; Marin-Beloqui, J. M. "Optoelectronic Studies of Methylammonium Lead Iodide Perovskite Solar Cells with Mesoporous TiO₂: Separation of Electronic and Chemical Charge Storage, Understanding Two Recombination Lifetimes, and the Evolution of Band Offsets during J–V Hysteresis". *Journal of the American Chemical Society* **2015**, *137*, 5087-5099.

Oga, H.; Saeki, A.; Ogomi, Y.; Hayase, S.; Seki, S. "Improved Understanding of the Electronic and Energetic Landscapes of Perovskite Solar Cells: High Local Charge Carrier Mobility, Reduced Recombination, and Extremely Shallow Traps". *Journal of the American Chemical Society* **2014**, *136*, 13818-13825.

Onoda-Yamamuro, N.; Matsuo, T.; Suga, H. "Calorimetric and IR spectroscopic studies of phase transitions in methylammonium trihalogenoplumbates (II)[†]". *J. Phys. Chem. Solids* **1990**, *51*, 1383-1395.

Onoda-Yamamuro, N.; Matsuo, T.; Suga, H. "Dielectric study of CH₃NH₃PbX₃

(X=CL, BR, I)". *J. Phys. Chem. Solids* **1992**, *53*, 935-939.

Pockett, A.; Eperon, G. E.; Peltola, T.; Snaith, H. J.; Walker, A. B.; Peter, L. M.; Cameron, P. J. "Characterization of planar lead halide perovskite solar cells by impedance spectroscopy, open circuit photovoltage decay and intensity-modulated photovoltage/photocurrent spectroscopy". *The Journal of Physical Chemistry C* **2015**, *119*, 3456–3465.

Poglitsch, A.; Weber, D. "Dynamic disorder in methylammoniumtrihalogenoplumbates (II) observed by millimeter-wave spectroscopy". *The Journal of Chemical Physics* **1987**, *87*, 6373-6378.

Qin, C.; Matsushima, T.; Fujihara, T.; Potscavage, W. J.; Adachi, C. "Degradation Mechanisms of Solution-Processed Planar Perovskite Solar Cells: Thermally Stimulated Current Measurement for Analysis of Carrier Traps". *Advanced Materials* **2016**, *28*, 466-471.

Roiati, V.; Colella, S.; Lerario, G.; De Marco, L.; Rizzo, A.; Listorti, A.; Gigli, G. "Investigating charge dynamics in halide perovskite-sensitized mesostructured solar cells". *Energy & Environmental Science* **2014**, *7*, 1889-1894.

Sanchez, R. S.; Gonzalez-Pedro, V.; Lee, J.-W.; Park, N.-G.; Kang, Y. S.; Mora-Sero, I.; Bisquert, J. "Slow dynamic processes in lead halide perovskite solar cells. Characteristic times and hysteresis". *The Journal of Physical Chemistry Letters* **2014**, *5*, 2357–2363.

Sepalage, G. A.; Meyer, S.; Pascoe, A.; Scully, A. D.; Huang, F.; Bach, U.; Cheng, Y.-B.; Spiccia, L. "Copper(I) Iodide as Hole-Conductor in Planar Perovskite Solar Cells: Probing the Origin of J–V Hysteresis". *Advanced Functional Materials* **2015**, *25*, 5650-5661.

Shi, D.; Adinolfi, V.; Comin, R.; Yuan, M.; Alarousu, E.; Buin, A.; Chen, Y.; Hoogland, S.; Rothenberger, A.; Katsiev, K.; Losovyj, Y.; Zhang, X.; Dowben, P. A.; Mohammed, O. F.; Sargent, E. H.; Bakr, O. M. "Low trap-state density and long carrier diffusion in organolead trihalide perovskite single crystals". *Science* **2015**, *347*, 519-522.

Stranks, S. D.; Burlakov, V. M.; Leijtens, T.; Ball, J. M.; Goriely, A.; Snaith, H. J. "Recombination Kinetics in Organic-Inorganic Perovskites: Excitons, Free Charge, and Subgap States". *Physical Review Applied* **2014**, *2*, 034007.

Sze, S. M. *Physics of Semiconductor Devices*, 2nd ed.; John Wiley and Sons: New York, 1981.

Tomozawa, M.; Shin, D.-W. "Charge carrier concentration and mobility of ions in a silica glass". *Journal of Non-Crystalline Solids* **1998**, *241*, 140-148.

Unger, E. L.; Hoke, E. T.; Bailie, C. D.; Nguyen, W. H.; Bowring, A. R.; Heumüller,

T.; Christoforo, M. G.; McGehee, M. D. "Hysteresis and transient behavior in current-voltage measurements of hybrid-perovskite absorber solar cells". *Energy & Environmental Science* **2014**, *7*, 3690-3698.

Wang, Q.; Shao, Y.; Xie, H.; Lyu, L.; Liu, X.; Gao, Y.; Huang, J. "Qualifying composition dependent p and n self-doping in CH₃NH₃PbI₃". *Applied Physics Letters* **2014**, *105*, 163508.

Wetzelaer, G.-J. A. H.; Scheepers, M.; Sempere, A. M.; Momblona, C.; Ávila, J.; Bolink, H. J. "Trap-Assisted Non-Radiative Recombination in Organic-Inorganic Perovskite Solar Cells". *Advanced Materials* **2015**, *27*, 1837-1841.

Wu, X.; Yu, H.; Li, L.; Wang, F.; Xu, H.; Zhao, N. "Composition-Dependent Light-Induced Dipole Moment Change in Organometal Halide Perovskites". *The Journal of Physical Chemistry C* **2014**, *119*, 1253-1259.

Xiao, Z.; Yuan, Y.; Shao, Y.; Wang, Q.; Dong, Q.; Bi, C.; Sharma, P.; Gruverman, A.; Huang, J. "Giant switchable photovoltaic effect in organometal trihalide perovskite devices". *Nat Mater* **2015**, *14*, 193-198.

Yang, T.-Y.; Gregori, G.; Pellet, N.; Grätzel, M.; Maier, J. "The significance of ion conduction in a hybrid organic-inorganic lead-iodide-based perovskite photosensitizer". *Angewandte Chemie International Edition* **2015**, *54*, 7905-7910.

You, J.; Meng, L.; Song, T.-B.; Guo, T.-F.; Yang, Y. M.; Chang, W.-H.; Hong, Z.; Chen, H.; Zhou, H.; Chen, Q.; Liu, Y.; De Marco, N.; Yang, Y. "Improved air stability of perovskite solar cells via solution-processed metal oxide transport layers". *Nature Nanotechnology* **2016**, *11*, 75-81.

Zaban, A.; Greenshtein, M.; Bisquert, J. "Determination of the electron lifetime in nanocrystalline dye solar cells by open-circuit voltage decay measurements". *ChemPhysChem* **2003**, *4*, 859-864.

Zarazua, I.; Bisquert, J.; Garcia-Belmonte, G. "Light-Induced Space-Charge Accumulation Zone as Photovoltaic Mechanism in Perovskite Solar Cells". *The Journal of Physical Chemistry Letters* **2016**, *7*.

Zhu, X. Y.; Podzorov, V. "Charge Carriers in Hybrid Organic-Inorganic Lead Halide Perovskites Might Be Protected as Large Polarons". *The Journal of Physical Chemistry Letters* **2015**, *6*, 4758-4761.